Cryogenic radiative cooling of a large payload for gravitational wave detector Design and results of the E-TEST project

Jacques, Lionel ; Zeoli, Morgane ; Amorosi, Anthony ; Bertolini, Alessandro; Collette, Christophe ; Cornelissen, Robin ; Di Fronzo, Chiara ; Habraken, Serge ; Loicq, Jérôme ; More Authors

DOI
10.1016/j.cryogenics.2025.104057

Publication date
2025

Document Version
Final published version

Published in
Cryogenics

Cryogenics 147 (2025) 104057

Contents lists available at ScienceDirect

Cryogenics

journal homepage: www.elsevier.com/locate/cryogenics

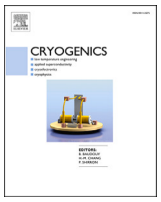

Cryogenic radiative cooling of a large payload for gravitational wave detector: Design and results of the E-TEST project

Lionel Jacques [a,*], Morgane Zeoli [b,c], Anthony Amorosi [b,d], Alessandro Bertolini [e], Christophe Collette [b,d], Robin Cornelissen [e], Chiara Di Fronzo [b,1], Serge Habraken [a], Joris V. van Heijningen [f,e], Gino Hoft [e], Robert Joppe [g], Tim J. Kuhlbusch [g], Mouhamad Haidar Lakkis [b,d], Bao Long Levan [a], Cédric Lenaerts [a], Jérôme Loicq [a,h], Benoit Marquet [a], Enrico Porcelli [e], Ameer Sider [b], Matteo Tacca [e]

[a] University of Liège, Centre Spatial de Liège, Avenue Pré-Aily, Liège Science Park, 4000, Belgium
[b] University of Liège, Precision and Mechatronics Laboratory, Allée de la Découverte 9, Liège, 4000, Belgium
[c] Centre for Cosmology, Particle Physics and Phenomenology (CP3), UCLouvain, Chemin du Cyclotron 2, B-1348, Louvain-la-Neuve, Belgium
[d] Université Libre de Bruxelles, Precision and Mechatronics Laboratory, Avenue F.D. Roosevelt 50, Brussels, B-1050, Belgium
[e] Nikhef, Science Park 105, 1098XG, Amsterdam, the Netherlands
[f] Department of Physics and Astronomy, VU Amsterdam, De Boelelaan 1081, 1081 HV Amsterdam, the Netherlands
[g] III. Physikalisches Institut, RWTH Aachen University, Otto-Blumenthal-Straße, 52074, Aachen, Germany
[h] Aerospace Faculty, Technische Universiteit Delft, Kluyverweg 1, 2629, HS Delft, the Netherlands

ARTICLE INFO

Keywords:
Gravitational wave detector
Einstein
E-TEST
Radiative heat transfer
Cryogenic

ABSTRACT

Third-generation gravitational wave detectors will use large mirrors isolated from seismic motion at low frequency, and also cooled down to cryogenic temperatures. To fulfil these two specifications, the E-TEST project explores the possibility of using a purely non-contact radiative cooling strategy. Based on cooling predictions, the paper includes a detailed design of the cryostat and the assembly procedure. A test campaign demonstrated that the proposed strategy succeeded in bringing the temperature of a 100 kg dummy mirror down to 22 K in 19 days. These encouraging results are paving the way toward a fully radiative approach for cooling the mirrors of the future Einstein Telescope.

1. Introduction

The sensitivity to gravitational-wave (GW) signals of existing ground-based observatories is limited at low frequencies, in particular around 10 Hz [1–3]. This limitation comes from several noise contributions, including the coupling of the mirror motion with other degrees of freedom, seismic noise, and thermal noise. The Einstein Telescope (ET) is a third-generation gravitational-wave detector aiming to mitigate these noise sources to broaden its sensitivity curve down to 3 Hz, thus significantly increasing the observable volume of the universe [4]. Thermal noise contributions from the mirror suspension and the mirror coating can be efficiently reduced by cooling the payload to cryogenic temperature, choosing a low-mechanical loss material for the mirror, and increasing the mirror mass. The low-loss material selected for ET cryogenic mirrors is silicon because of its numerous advantages at cryogenic temperatures. Silicon's mechanical losses decrease with temperature, it has high thermal conductivity, and its coefficient of thermal expansion (CTE) is null around 123 K and becomes very close to zero below 18 K [5,4,6–8]. At these two zero-CTE points, the thermoelastic noise component to the thermal noise vanishes and the distortions of the mirror due to thermal-induced stresses are minimized. For this reason, ET is planned to operate in the 10–20 K range. Cooling the payload of gravitational-wave detectors is not straightforward and must meet two requirements: (i) an efficient thermal link between the payload and the cooling system must be ensured to guarantee an efficient extraction of the absorbed heat on the mirror from the high-power incoming laser and remaining parasitic radiative heat load from the environment, (ii) the seismic isolation must be preserved by mechanically isolating the pay-

* Corresponding author.
E-mail address: ljacques@uliege.be (L. Jacques).
[1] New affiliation: OzGrav, University of Western Australia, Crawley, Western Australia 6009, Australia.

https://doi.org/10.1016/j.cryogenics.2025.104057
Received 20 December 2024; Received in revised form 21 February 2025; Accepted 10 March 2025

Available online 13 March 2025

Nomenclature

CLIO	Cryogenic laser interferometer observatory	He-II	Superfluid helium
CSL	Centre Spatial de Liège	HLVIS	Heat-link vibration isolation system
CTE	Coefficient of thermal expansion	IP	Inverted Pendulum
E-TEST	Einstein Telescope Euregio Meuse-Rhine Site & Technology	IR	Infrared
		KAGRA	Kamioka Gravitational wave detector
ET	Einstein Telescope	LF	Low Frequency
FEA	Finite Element Analysis	LIGO	Laser Interferometer Gravitational-Wave Observatory
FOCAL	Facility for Optical Calibration at Liège	LN_2	Liquid nitrogen
GAS	Geometric Anti-Spring	MLI	Multi-Layer Insulation
GHe	(Gaseous) Helium	PCTFE	Polychlorotrifluoroethylene
GW	gravitational wave	PTFE	Polytetrafluoroethylene

load from the cooling system [4]. As a baseline requirement for ET, the vibrations of the payload cooling system must be attenuated to a lower level than what the seismic isolation chain can achieve, which is of the order of 2×10^{-18} m/$\sqrt{\text{Hz}}$ at 2 Hz for a 10 km arm [9]. The laser heat load is expected to be in the 0.1–1 W range, setting the requirement on the cooling power of the cryogenic system at the operating temperature, between 10 and 20 K [4,9].

1.1. State of the art

The Einstein Telescope is not the only gravitational-wave detector aiming to operate at cryogenic temperature. Low-vibration cooling systems are developed worldwide for other facilities, such as KAGRA (Kamioka Gravitational wave detector) and LIGO (Laser Interferometer Gravitational-wave Observatory) Voyager. This section reviews and compares the low-vibration cooling strategies designed for various GW detectors. It is important to note that all these systems were not designed based on the same requirements.

Similarly to the Einstein Telescope, the Japanese GW observatory KAGRA is designed to operate at 20 K. Their strategy is to cool the detector monocrystalline sapphire mirrors with conductive cooling [3] through high thermal conductivity and low stiffness 6N (99.9999%) pure aluminum heat links [10]. Four 1 W pulse-tube cryocoolers sustain the 8 K and 80 K thermal shields surrounding the payload. Pulse-tube cryocoolers were selected as they proved to be the lowest-vibration alternating regenerative cryocoolers. The vibration level at their cold-head is two orders of magnitude lower than those of Gifford-McMahon coolers [11–13]. The additional relative vibration between the cold head and the cold-end stage that comes from thermal deformation and pressure waves in the cryocooler body is of the same order of magnitude for both types of coolers [11]. To limit vibration transmission through heat links and maintain stringent seismic isolation requirements, thermal shields are connected to an upper stage of the suspension, and an additional multistage heat-link vibration isolation system (HLVIS) is used for further decoupling. A similar strategy is implemented for the cryogenic laser interferometer observatory (CLIO), located in the Kamioka Mine, alongside the KAGRA detector. They tested a 4 K and a 80 K pulse-tube cooling system that both exhibit vibration amplitudes of the cryocooler less than 1 μm (comparable to the seismic motion in the mine) while achieving a temperature of 4.5 K and 70 K with a cooling power of 0.5 W and 50 W, respectively [14,15]. This strategy is efficient in sustaining low cryogenic temperatures. Still, it comes with a great toll in terms of suspension design complexity to avoid transmitting the cryocooler vibration to the detector test mass and spoiling the seismic isolation performance.

The future American GW detector LIGO Voyager steps away from this convoluted strategy and prefers radiative cooling [6,16]. It plans to operate at 123 K, one of the zero-CTE points of low-loss crystalline silicon material. Their design consists of two non-contacting cylindrical cold shields surrounding the test mass at the last stage of the suspension of the detector seismic isolation chain. The inner shield operates at a temperature of 83 K and maintains the mirror temperature by radiatively absorbing the expected 5 W steady-state heat load from the mirror. It is coated with a high emissivity black coating to maximize the radiative coupling to the test mass. The second shield has a temperature of 80 K and protects the inner shield from additional heat load from radiation emitted by the surrounding room temperature environment. The shields being mechanically decoupled from the test mass avoids direct vibration transmission to the mirror. However, the inner thermal shield is still subjected to low vibration requirements. Indeed, it has a direct view to the laser beam and if a small fraction of the scattered light sees a vibrating surface, it is translated into a phase shift on the light when recombining at the mirror level. This can then cause disturbances in the radiation pressure on the mirror coming from the light, leading to a reduction in the sensitivity of the detector. The low vibration requirement is met by suspending the inner shield from an active isolation platform. The outer shield is cooled by a Gifford-McMahon cryocooler, whose vibrations can be attenuated with spring-mass systems but are not critical since the outer cryostat does not see the laser beam. The inner shield is conductively cooled by a flexible copper heat link attached to the outer shield. The radiative cooling is efficient for maintaining the mirror at 123 K but would require a long time to cool it from room temperature. The primary cool-down is thus completed conductively by connecting a movable heat link to the mirror, which is removed as soon as the operating temperature is reached. A demonstrator was built, tested and proved that this technique allowed to cool a mirror to 124 K without impacting its vibration isolation [16].

The low-vibration cooling strategy for ET has not yet been determined, and different technologies are being studied across Europe to determine the most appropriate one. This implies a strategy that could provide the required cooling power while preserving the detector seismic isolation, with limited design complexity, cost, and maintenance. ETpathfinder [17] is a research facility in Maastricht developing key technologies for ET and is investigating an improved version of the KAGRA conductive cooling strategy via low-stiffness heat-links and low-vibration cryocoolers. The difference lies in the active cooling strategy. Traditional cryocoolers can be made low-noise with sophisticated vibration reduction systems as in KAGRA, but they will always produce vibrations because of their mechanical compressor. In ETpathfinder, a sorption-based Joule-Thomson cooler is chosen for the active cooling. Sorption compressors are thermally driven and use passive valves to direct the gas flow direction [18,19]. The absence of moving parts in the compressor (besides the passive valves) makes them almost vibration-free. ETpathfinder demonstrator should thus be able to reduce all fundamental noise sources down to 1×10^{-18} m/$\sqrt{\text{Hz}}$ from 20 Hz onwards. However, sorption coolers cooling capacity depends on the nature of the cryogen flowing in the cycle and it requires more cooling stages than traditional cryocoolers making the overall cooling system even more complicated than KAGRA's. The ETPathfinder cryostat design is composed of four nested thermal shields: (i) an outer thermal shield at 250 K, (ii) a liquid nitrogen (LN_2) shield at 80–90 K, (iii) an interme-

diate neon (Ne) shield at 40 K, and (iv) an inner helium (He) shield at 15 K. It is composed of a cascade of three sorption cooler stages: a Ne stage providing 2.5 W cooling power and cooling the 40 K shield, a He stage with 0.5 W cooling power and cooling the 15 K shield, and a H_2 stage at 8 K, which, combined with the aluminium heat links, provide a cooling power of 50 mW for the payload. Since sorption coolers are effective in maintaining a given temperature but not for cooling down a massive system from room temperature, the cooling of the payload is performed in two steps. During the first step, the payload is cooled from room temperature to the sorption cooler working temperature range by a powerful LN_2 cooling system and a convective helium gas loop cooled by a traditional vibrating mechanical cooler. Once the operating temperature of 10 K is reached, the pre-cooling system is deactivated and the sorption-based Joule-Thomson cooler is switched on.

Another idea considered for ET cooling system, or at least its future version, is to make use of the superfluid helium (He-II) at 2 K. Future versions are mentioned because He-II implies a mirror working temperature of 10 K rather than 20 K. He-II displays an extremely low viscosity and very high specific heat, which prevents small transient temperature fluctuation [9]. In addition, its steady-state thermal conductivity is one order of magnitude larger compared to the best solid conductive material [20], which makes it able to extract heat a thousand times better than any metallic conductor [9]. This high thermal conductivity allows for a fast cooling of the payload without a significant thermal gradient along the cooling lines and there is no need for macroscopic He-II flow, leading to an extremely low vibration system. This ultra-low noise cooling would allow for a detector sensitivity below 1×10^{-20} m/$\sqrt{\text{Hz}}$ in the detection band [20]. He-II is generated by pumping from a regular He-I bath, which is supplied by a cryoplant. The latter must be installed in a separate cavern since it still has vibrating components such as a compressor. Additional 1.8 K units for liquefaction and refrigeration units must be placed in the main cavern to sustain the He-II cooling. Another advantage of He-II cooling is that, unlike regular cryocoolers, a single helium refrigerator can provide cooling capacity to all cryostats of ET [20,4].

1.2. Context and scope

A third cooling strategy for ET is investigated in the context of the E-TEST collaboration (Einstein Telescope Euregio-Meuse-Rhin (EMR) Site and Technology) [21,22]. This project is dedicated to developing technologies necessary for 3rd generation gravitational-wave detectors. It focuses on the suspension and low-frequency isolation of a large cryogenic mirror. A new low-vibration cooling strategy was developed for the E-TEST prototype. Similar to LIGO Voyager, E-TEST steps aside from conductive cooling and its complex thermally conductive heat paths and focuses on radiative cooling. The low-vibration requirements of the inner part of the radiative heat exchanger are met by suspending it to the last stage of the seismic isolation chain (cold platform), right above the test mass. An external cryostat is actively cooled and is completely disconnected from the rest of the prototype. The non-contact radiative cooling between the external and internal cryostat ensures a complete mechanical decoupling between the cooling system and the test-mass, preserving the vibration isolation while maintaining the cryogenic environment. The cold platform is equipped with five cryogenic inertial sensors to monitor the residual vibration remaining at the test mass level. The cryostat developed in the E-TEST project bridges the gap between 123 K and 20 K left by LIGO Voyager by maximizing the radiative heat exchange area between the suspended payload and the actively cooled environment with interleaved fins.

It is important to note that E-TEST is a technology demonstrator. It aims at proving the feasibility of radiative cooling and is thus not designed to directly meet ET's specifications in terms of cooling power and displacement noise at the payload level. The absence of laser heating the mirror indeed relaxes the requirements for the cooling power. Once demonstrated, the design can be upscaled to meet ET's requirements.

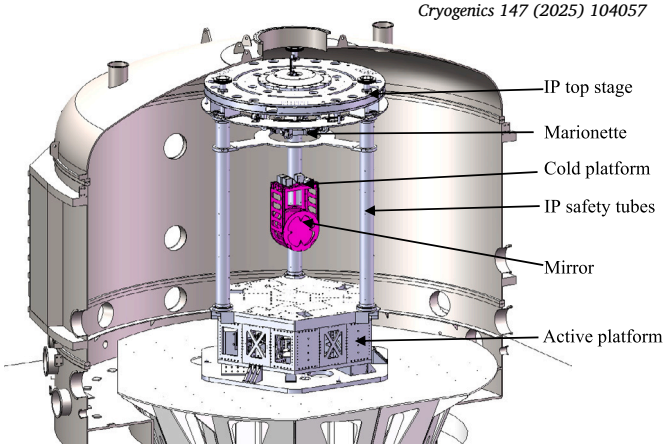

Fig. 1. Prototype inside the FOCAL6.5 vacuum chamber with the active platform, inverted pendulum, marionette, cold platform and mirror. (For interpretation of the colours in the figure(s), the reader is referred to the web version of this article.)

To take advantage of the existing expertise and infrastructure available in the EMR region, the E-TEST prototype was integrated in existing facilities at the Centre Spatial de Liège (CSL).

The cryostat design is described extensively in the following sections. Section 2 starts with a preliminary steady state assessment of the required area and then describes the subsequent detailed design of the cryostat. Section 3 then presents the model and associated cooling predictions while Section 4 describes the hardware and test results. The model is eventually correlated in Section 5 before presenting conclusions, lessons learnt and future work.

2. Cryostat design

2.1. Problem statement

The overall objective is to radiatively cool down the payload, *i.e.* a 100 kg 450 mm diameter silicon mirror and its supporting cold platform (in pink in Fig. 1). The main idea is therefore to provide an actively cooled radiative environment surrounding the cold platform and mirror. A sufficiently large radiating area has to be connected to the cold platform since the mirror cannot be considered as interface, facing the actively cooled environment. In the frame of E-TEST, the available volume is bounded by the active platform, the top stage of the inverted pendulum (IP) and the feet of the IP, as depicted in Fig. 1. It is further bounded by the existing 6.5 m diameter vacuum chamber of CSL planned to be used for the test: FOCAL6.5 (Facility for Optical Calibration at Liège) vacuum chamber. The cold platform hosting the mirror is suspended through 3 titanium wires from the marionette, itself suspended from the keystone of a geometric anti-spring (GAS) filter mounted at the center of the inverted pendulum top stage. In the ET interferometer, a large optical aperture is required to illuminate the whole mirror. In E-TEST, due to the bounded environment, large thermal baffling for a large aperture was not possible, but it is not considered as critical for ET. Indeed, the length of the thermal baffle only needs scaling up to limit the radiative heat load. To still enable optical measurement of the mirror, 3 small apertures are required in front of the mirror instead of one single large aperture.

2.2. Preliminary steady-state equilibrium

One of the driving constraints in the radiative heat exchanger design is the area required to achieve a sufficiently low temperature. As a first approximation, the average steady-state temperature of the payload is governed by the following equation, assuming two parallel plates of area A and emissivity ϵ:

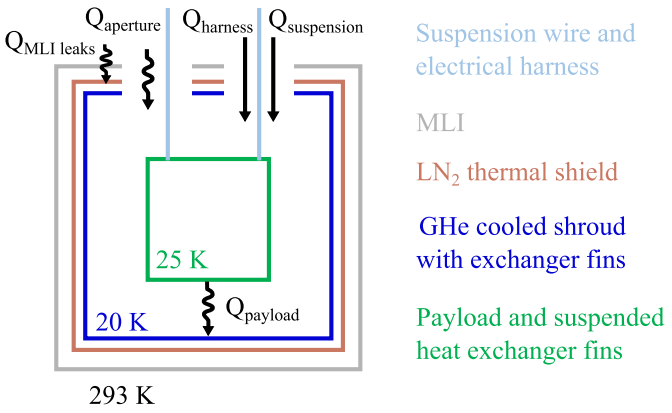

Fig. 2. Heat transfer flowing in the system. The straight arrows are conductive heat transfers and the waving arrows are radiative transfers.

Table 1
Heat load assessment summary.

	Q [mW]
Apertures	50
MLI leaks	50
Suspension wires	100
Harness	50

$$Q_{\text{payload}} = \sigma \frac{A\epsilon}{2-\epsilon}(T^4_{\text{payload}} - T^4_{\text{sink}}) \tag{1}$$

where Q_{payload} is the total heat to be evacuated from the payload, T_{payload} the payload temperature, T_{sink} the actively cooled environment temperature and σ Stefan-Boltzmann's constant.

First, the required cooling power Q_{payload} is assessed by listing the various heat loads affecting the payload. To limit the heat load on the payload from the environment, the outer cryostat architecture is composed of a main support structure at ambient temperature, supporting an external liquid nitrogen (LN_2) thermal shield. The actively cooled panels are mounted on this LN_2 shield, and are fed with gaseous helium (GHe) from the CSL closed-loop helium refrigerator. GHe panels are mounted on the LN_2 shield to limit the external heat load to the helium refrigerator. As water contamination is not an issue in the frame of E-TEST prototype, classical Multi-Layer Insulation (MLI) is used around the GHe panels and around the LN_2 panels to further reduce the heat load. The main sources of heat to be evacuated from the mirror and cold platform:

- Radiative heat load from nominal apertures (suspension wires, optical apertures)
- Radiative heat load from holes & defects in MLI
- Conductive heat load from the suspension wires
- Conductive heat load from the payload electrical harness (temperature sensors, vibration sensors)

They are illustrated in Fig. 2. The total heat load to the payload can be estimated to around 250 mW, as summarized in Table 1. The assessment of the individual heat loads is detailed in Appendix A. For ET, the additional load from the laser beam partially absorbed by the mirror is expected in the 0.1–1 W range and strongly depends on the water layer that might be adsorbed on the front face of the mirror [20].

The emissivity plays a significant role in the heat load extraction from the payload but usually decreases with temperature, as discussed in more details in Section 3. Based on Equation (1) and considering conservatively an emissivity of 0.4 with the temperature of the GHe-cooled panels at 20 K, the required area to evacuate the 250 mW would

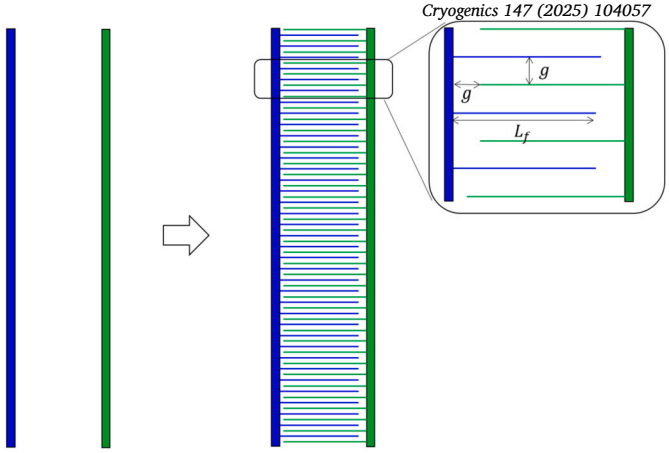

Fig. 3. Compact radiative heat exchanger concept, based on interleaved fins.

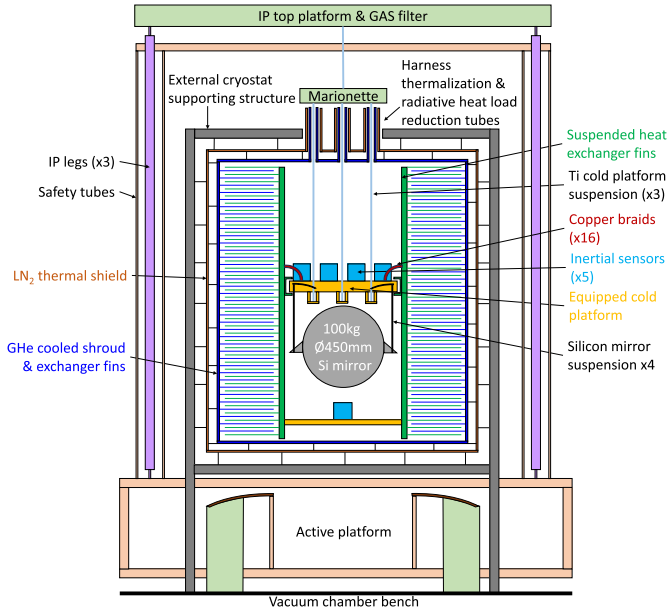

Fig. 4. Cryostat and radiative heat exchanger initial architecture with vertical stacking (front view), integrated in the suspension chain. The test-mass is a 100 kg silicon mirror.

be 75 m^2 for a target temperature of 25 K. The following subsection proposes a solution to fit this required area in the available volume.

2.3. Compact heat exchanger concept

Several geometries were investigated to make a compact radiative heat exchanger, such as interleaved honeycomb, tubes and planar fins. Interleaved fins as described in Fig. 3 exhibit the best total-to-projected area ratio or amplification ratio. This ratio is defined by:

$$\frac{A_t}{A_p} = 1 + \frac{L_f}{g} \tag{2}$$

with A_t the total radiating area of one side, A_p the projected area of one side, L_f the fin length and g the gap between passive (suspended) and actively cooled fins. The same gap g is considered between the tip of the fin and the opposite panel.

Applying the above-described heat exchanger concept, two types of configurations can be investigated: vertical or horizontal stacking. The vertical stacking configuration is described in Fig. 4. On the suspended cold platform (in yellow) is mounted a structure to support the fins (in green). The outer part of the radiative heat exchanger is com-

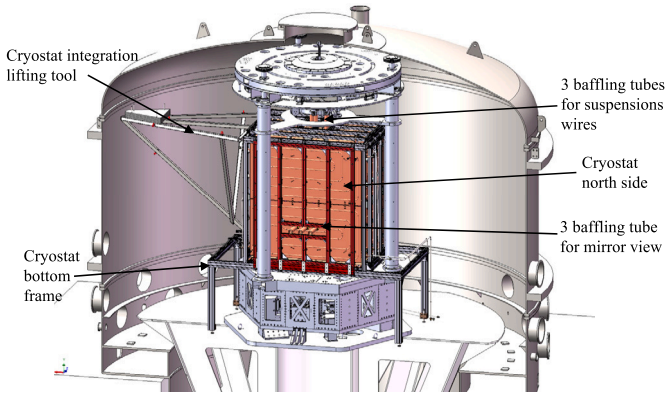

Fig. 5. Prototype CAD view, with the cryostat closed in between the IP legs, above the active platform.

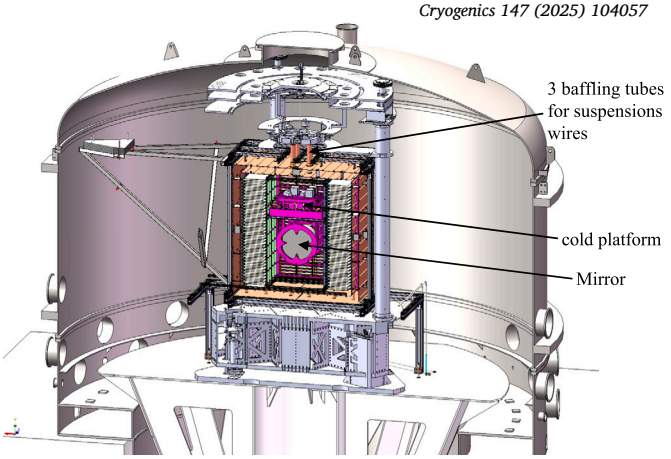

Fig. 6. Prototype CAD cut view, showing the inner details of the radiative heat exchanger integration with the suspended payload.

posed of an external supporting structure (in grey) lying directly on the ground without contact with the active platform. This structure supports the LN_2 thermal shield (in brown). The vertical LN_2 panels host the GHe panels onto which the external fins are fixed (in blue). This configuration allows some in-plane and vertical translations, within the inter-fin gap fixed at 20 mm. This allocated clearance takes into account various thermo-mechanical effects that will be further explained in section 2.4.3. Four cryogenic inertial sensors (cyan) were integrated on the cold platform (two verticals and two horizontals), with an additional horizontal one below the mirror. They are used to monitor the residual translation and pitch of the cryogenic payload. Alternative horizontal stacking configurations might provide more benefit in terms of degrees of freedom and amplification ratio. One advantage of horizontal stacking, the fins being vertical, is to mitigate the bending of the fins under their own weight, therefore allowing longer fins and amplification ratio. Limitation from buckling should nevertheless be considered for the fins pointing upwards. Circular vertical fins could mitigate buckling. A horizontal configuration would, for instance, provide an amplification ratio about 70 with 700 mm long fins, enabling 500 m^2 total heat exchanger area and therefore reaching a payload temperature of 13 K with a sink at 4 K (for 250 mW heat load and same emissivity of 0.5).

2.4. Detailed design

The selected configuration was vertical stacking because of practical implementation constraints. For similar reasons, cooling the active side to liquid helium temperature with the existing facilities at CSL was discarded. Therefore, the helium refrigerator provides a 15–20 K environment. Increasing the total exchanger area would not allow cooling below 20 K.

In practice, 35 layers of 300 mm long fins, 800 mm wide for the short ones and 1100 mm wide for the long ones were implemented and led to a total developed heat exchanger area of almost 80 m^2. The suspended payload is a 100 kg silicon mirror, suspended by four silicon suspension fibres. For the first test campaign, the test-mass is replaced by a dummy mass made of aluminium, and suspension rods made of CuCrZr (C18150) alloy. To compensate for the change in density, the thickness of the dummy mass was adapted to keep the 450 mm diameter.

As the size of the cold platform is fixed by the 450 mm diameter of the mirror and the overall structure of the cryostat must fit in between the IP legs, the length of the fins is limited. Fig. 5 and 6 show how the concept was implemented in the prototype. The external part of the cryostat is supported by a frame stepping over the active platform to interface directly with the vacuum chamber floor. One side of the cryostat is equipped with three aperture baffles, allowing a direct view of the mirror dedicated to optical experiments, while limiting the heat load. The baffles are composed of one external tube mounted on the LN_2 shield and one internal tube mounted on the GHe-cooled panel. The length of

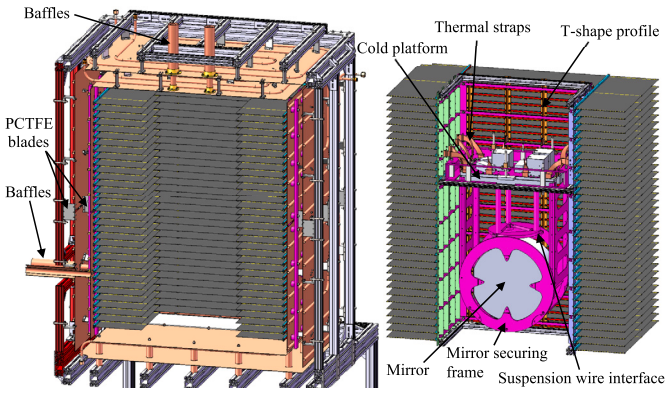

Fig. 7. Detailed design of the cryostat with the active side of the radiative heat exchanger mounted on the actively-cooled panels (left) and the suspended payload with the inner side of the radiative heat exchanger (right).

the internal tube is 400 mm. Similarly, the apertures for the three suspension wires on the top side are also equipped each with a set of two tubes, the outer one at LN_2 temperature and the inner one at GHe temperature. They offer baffling of the IR radiation and radiative thermalisation of suspension wire and electrical harnesses. The electrical harnesses of the temperature and mechanical sensors located on the cold platform and inner side of the radiative heat exchanger, are made of phosphor bronze for its low thermal conductivity. The assumed total cross section is equivalent to 20 × AWG 24 (0.2 mm^2) wires for the mechanical sensors and 100 × AWG 32 (0.032 mm^2) wires for the temperature sensors. The wires are twisted along the suspension cables through the top tubes. Twisting the wires increases their surface exposed to the tubes to maximise radiative thermalisation.

Fig. 7 shows the details of the cryostat. On the suspended part of the radiative heat exchanger, one of the main design driver is the vertical location of the suspension wire bottom interface. It should lie within the plane of the centre of mass of the suspended payload. To enable some adjustment and meet this requirement, the cold platform is mounted inside a U-shaped profile with three adjustment screws. This allows not only to adjust the overall centre of gravity of the inner fins structure but also to adjust the pitch and roll angles. The thermal contact between the cold platform and the aluminium structure hosting the fins is therefore very poor. Additional flexible copper thermal braids are therefore implemented to circumvent this poor thermal contact. They provide direct connection between the T-shaped profiles onto which the fins are mounted and the cold platform. The T-shaped profiles conduct vertically the heat from the fins towards the thermal braids interfaces. As ensuring good thermal contacts is critical for the cooling efficiency, standard

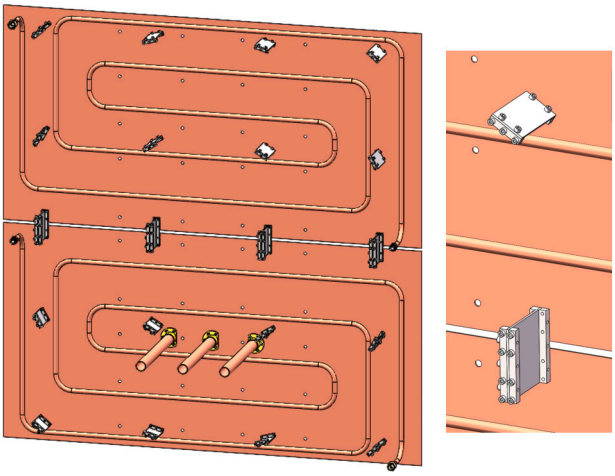

Fig. 8. GHe panels PCTFE blades design.

A2-70 stainless steel screws combined with Belleville washers are used to maintain the preload in the screws when cooling down. During the integration, the bottom side of the cryostat has to support the weight of the complete payload before it is suspended, the panels are supported by thick permaglas cylinders rather than thin blades like the lateral panels.

2.4.1. Outer cryostat panels support design

To limit the heat load on the helium refrigerator, the external cryostat helium panels are mounted on the LN_2 shield through insulating blades made of PCTFE (Polychlorotrifluoroethylene). This material is selected for its high stiffness to thermal conductivity ratio, and its better resistance to creep compared to classical PTFE (Polytetrafluoroethylene). For mechanical reasons, the blades were distributed as depicted in Fig. 8 with four vertical wider blades at the centre supporting most of the weight and 16 narrower blades pointing towards the centre of the two copper panels. This configuration allows for differential thermal contraction between the GHe panels and the external LN_2 panels supporting them without changing the centre position during contraction. Allocating a total conductive heat load of 1 W for each side and considering the effective length of the blade to be 75 mm (95 mm in total but 75 mm in between stainless steel clamps), the blades thickness is set to 3 mm with 4 blades of 100 mm width and 16 of 50 mm width. Mechanical analyses were then conducted to confirm sufficient margin of safety remained.

The same principle is applied for the blades linking the LN_2 panels to the external structure, knowing the heat load on the LN_2 was less critical but the mass to be supported (LN_2 + GHe + fins) is obviously larger. The thickness of the blade is thus increased to 8 mm, while their length is decreased to 70 mm (50 mm effective) for compactness.

2.4.2. Fin geometry sizing

As already mentioned in previous sections, the fin design results from trade-off between:

- Self-supporting capability (stiffness)
- Sufficient thermal conduction from tip to base
- Thermal capacity minimisation (to limit cool down duration)
- Manufacturing costs and availability
- High-emissivity coating compatibility

Due to the volume available in-between the inverted pendulum legs and the thickness of the external cryostat, the length of the fins is fixed to 300 mm. To minimise the weight while ensuring a sufficient thermal cross-section, a thickness of 0.2 mm of 1050A aluminium (99.5% purity) is selected. Even if high-purity aluminium exhibits higher thermal conductivity, the mechanical properties are poorer. The bending of 0.2 mm thick, 300 mm long fins is too excessive (>10 mm), and increasing the thickness would increase the overall thermal capacity. To overcome this issue, two main concepts were investigated: a self-supporting corrugated geometry and a flat geometry combined with a stiffening support structure.

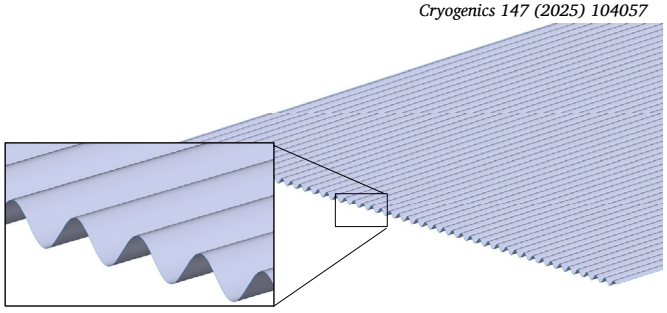

Fig. 9. Corrugated fin with a 2 mm peak-to-peak and 2 mm pitch profile.

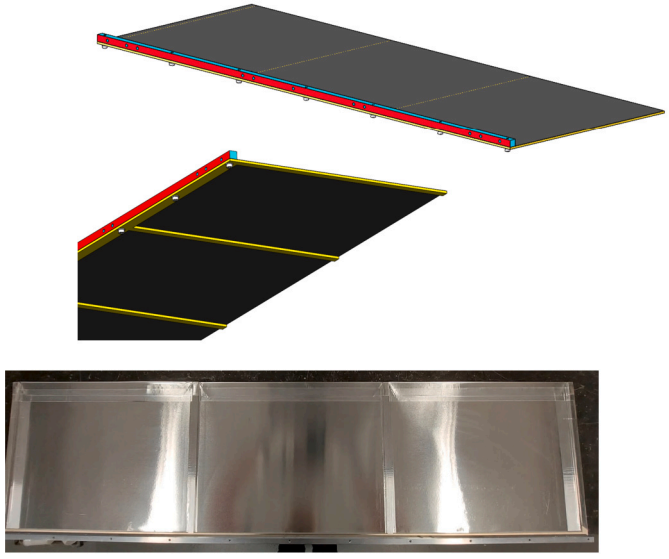

Fig. 10. Top: Flat fin + stiffener concept, with the stiffening fork in yellow and the base rod in red and cyan. Bottom: Picture of the as-built configuration, before painting.

The corrugated geometry offers several advantages. First the sine wave function increases the apparent stiffness of the fin: for a 2 mm pitch and 2 mm peak-to-peak sine, the deflection at the tip of the fin is below 1 mm, as depicted in Fig. 9. The second advantage is the light trapping or "macro-roughness" feature that increases the apparent emissivity of the fin at low temperature. Extending the concept further, micro-structuring of the fin could increase the apparent emissivity by matching the structure characteristic length to the peak black body emission wavelength. However, corrugated geometry implies an increase of mass for a given sheet thickness, roughly factor 1.5 for the above-described geometry. This might still be compensated by reducing the thickness since the overall stiffness is improved so that an optimum might be found. The main drawback of the corrugated fin lies in the difficulty of clamping the base and attach it to the main structure.

The second concept, presented in Fig. 10, is based on a fork-shaped stiffening secondary structure located below the 0.2 mm thick fin to limit the bending. The thickness of the stiffener and the spacing between the fork arms are designed to limit the overall deformation below 2 mm. The spacing between the forks is about 300 mm and their thickness is 3 mm. The foil is attached to the fork through low-outgassing aluminium tape and it is clamped at the base between the fork base and a $10\times10\,mm^2$ extruded aluminium rod. This rod also serves as interface with the rest of the structure.

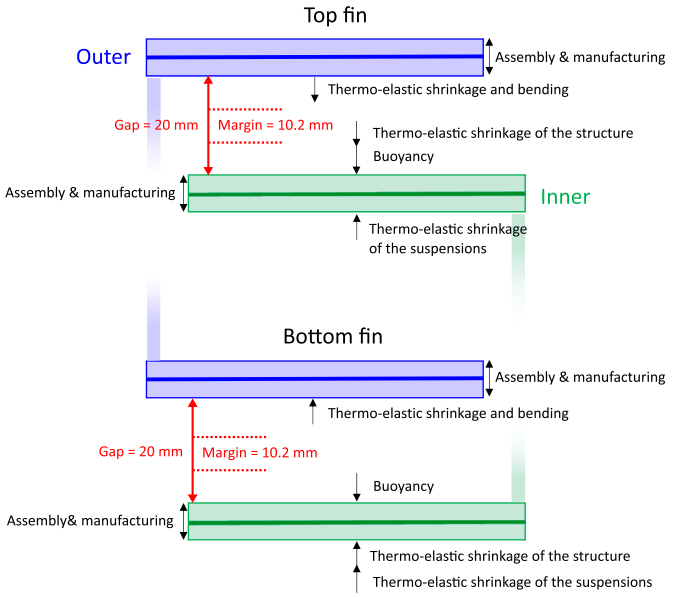

Fig. 11. Inter-fin gap tolerancing analysis summary for the top and the bottom of the radiative heat exchanger.

The main drawback of the flat foil is its proneness to plastic deformation generating bumps. The manufacturing process of the fork also has the tendency to leave manufacturing stresses that sometimes relax during the fin assembly and painting process, therefore inducing deformations. To further limit tip deformations, additional bent aluminium foil was applied.

The flat configuration was selected for the initial test run of the prototype. The corrugated version should be investigated further to overcome the assembly difficulties as its performances are expected to be better.

2.4.3. Gap sizing

Several contributors constrain the required clearance between the internal and external fins. The suspended radiative heat exchanger (inner cryostat) is subjected to global shrinkage because of the large CTE of its aluminum structure. The shrinkage of the three titanium suspension wires also impacts the gap sizing as it makes the suspended heat exchanger move upwards. Another significant contributor that influences the final location of the inner cryostat is the absence of buoyancy force in vacuum conditions. The inner cryostat being suspended and in equilibrium, when the air is pumped out of the vacuum chamber, it removes the vertical force due to Archimedes' law, directed upwards and equal to the removed volume of the inner cryostat and marionette.

The outer cryostat is subjected to thermo-elastic effects as well. The use of several different materials, mainly the fin structure made of aluminium and the GHe panels made of copper, does inevitably introduce large distortions. To mitigate these effects, the copper panel is sandwiched in-between the aluminium fin structure and an additional aluminium bar at the back of the panel, helping to keep the GHe panel flat. However, the combination of the GHe panels shrinkage and bending still needs to be taken into account in the inter-fin gap sizing.

On top of the predictive deformations, many statistical contributors also affect the gap between the fins due to manufacturing and assembly tolerances.

The various contributions to the clearance between the suspended and external fins of the exchanger are summarised in Fig. 11. They are quantified in Appendix B. In total, considering the allocated clearance of 20 mm between the fins, a margin of 10 mm is expected.

2.4.4. Residual gas molecular heat conduction

The expected operational distance between the fins being of the order of 10 mm, it becomes important to assess the potential impact of residual gas pressure heat transfer on the cooling process. The typical pressure achieved in that vacuum chamber is 1×10^{-6} mbar. However, this is the pressure measured at the chamber wall level and is not representative of the local pressure in the vicinity of the fins. Thanks to the different cryopumping mechanisms, the partial pressure of N_2, O_2 and Ar in the vicinity of the fins at an average temperature of 20 K drops well below 1×10^{-9} mbar [23,24]. At this level of pressure, even if it increases as the temperature decreases, the mean free path of the gas molecules remains several orders of magnitudes larger than the inter-fin distance. For instance, the mean free path of Nitrogen at 1×10^{-6} mbar is about 60 m and 4 m at 300 K and 20 K, respectively and increases by a factor 1000 at 1×10^{-9} mbar. The Knudsen number, being the ratio between the mean free path and the distance between the fin in our case, is very large and suggests the heat transfer regime between the fins is free molecular conduction. In that regime, the heat exchange between two surfaces, 1 and 2, is proportional to the local pressure [25,26]:

$$Q_{\text{gas cond}} = \frac{\gamma+1}{\gamma-1}\sqrt{\frac{N_A k_B}{8\pi M T_{\text{avg}}}}\, P F_a F_{12} A_1 (T_2 - T_1) \tag{3}$$

where γ is the specific heat ratio of the gas, M its molar mass, N_A Avogadro's number, k_B Boltzmann's constant, T_{avg} the average temperature $(T_1+T_2)/2$, F_{12} the view factor between the two surfaces and A_1 the fin area in our case. F_a is the accommodation coefficient factor and depends on the accommodation coefficients α_1 and α_2, depending themselves on the temperature of surfaces 1 and 2 and are analogous to the emissivity in radiative heat transfer. For parallel plates with unit view factor and conservatively assuming unit accommodation coefficients, F_a also becomes equal to 1 [25]. Considering a 5 K ΔT, an average temperature of 20 K and a partial pressure of N_2 of 1×10^{-9} mbar, the total heat exchange through free molecular gas conduction between the 80 m^2 fin area is of the order of μW and therefore several orders of magnitudes less than radiative heat transfer.

Following the above principle, taking advantage of molecular conduction to accelerate the colling of the payload was investigated. A controlled filling of the chamber or cryostat with a small helium pressure of the order 1 mbar could create a significant heat transfer. This well-known technique was used in past projects to for instance accelerate the cryogenic thermal cycling of the solar panels for the JUICE space mission [27]. Although very effective, this technique was eventually discarded as it did not seem practical and scalable to ET. It would for instance probably require specific gate valves to separate the ET-LF tower filled with helium from the beam pipe and dedicated pumping systems. Helium would also most probably leak into the warm part of the ET-LF tower. As described in Section 4.2, the technique was only used to accelerate warm-up.

3. Cooling predictions

3.1. Thermal model description

Based on the above-described design, a detailed thermal model was derived. The model is developed in the ESATAN-TMS software used for spacecraft thermal analysis, as depicted in Fig. 12. This software, based on the lumped parameter (finite difference) method, is particularly suited for such models since it enables complex radiative heat transfer modelling through ray-tracing including multiple-reflections. It also allows complex geometry modelling while limiting the number of nodes and therefore computation time for long transient simulations. The mirror is for instance modelled with one node, like the cold platform. The fins are discretised with 10 nodes in one direction from base to tip as the temperature gradient along the width of the fins is by design negligible. In total, the model is made of less than 400 nodes. Conduction through complex geometries are nevertheless modelled accurately

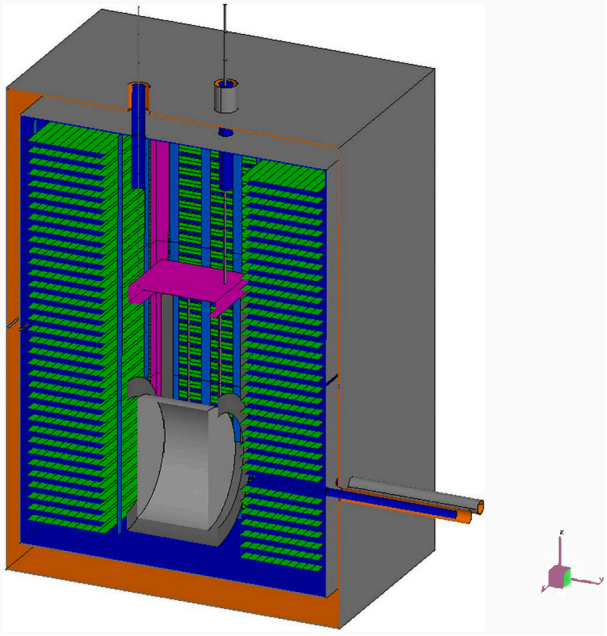

Fig. 12. Cut view of the ESATAN Geometrical Mathematical Model.

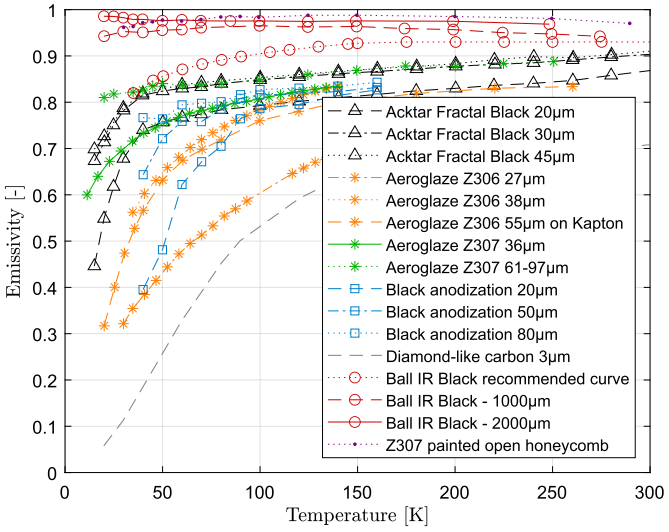

Fig. 13. Emissivity in function of temperature and thickness for various black coatings. Data extracted from [30–35].

with FEA to derive proper conductive links between the nodes. Contact through bolted connections are also taken into account and considered in the uncertainty analysis developed in Section 3.2.3.

Temperature-dependent thermal properties are used and based on standard data from NIST [28] and Touloukian [29]. Like any model, it is subject to high uncertainties, in particular when dealing with temperature-dependent properties. The emissivity of the fin black coating plays a significant role in the cooling performances while it is highly uncertain. Fig. 13, compiling data from various references [30–35], highlights that the emissivity of most of the black coatings exhibits a significant drop at low temperature, except for some very specific thick coating (like the Ball InfraRed Black™ developed for the James Webb Space Telescope cryogenic radiators but the thickness of this coating is in the millimetre range). This drop strongly depends on the coating thickness and therefore application process.

To be conservative in terms of cooling time, a constant emissivity, corresponding to low-temperature value, is used. The emissivity being

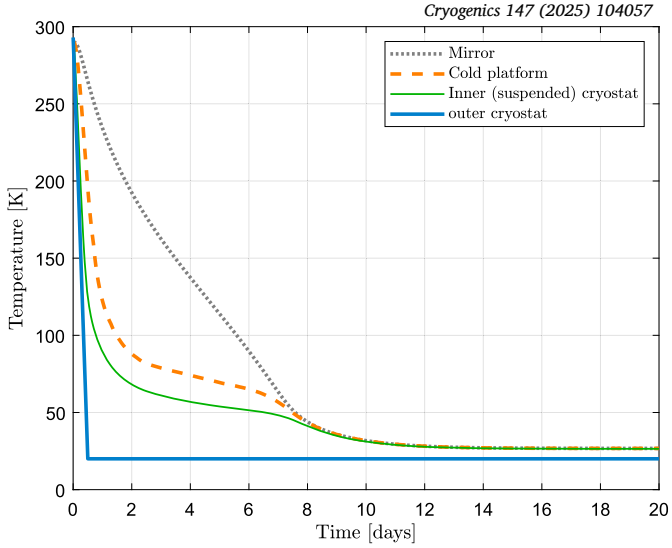

Fig. 14. Mirror, cold platform and inner suspended cryostat temperature profile with nominal properties.

higher at ambient temperature, it provides better heat exchanger performance during the beginning of the cooling. The effect of the temperature dependency was assessed in ESATAN using the piecewise grey-body method and confirmed the expected behaviour. It also showed that variations of the cooling profile with respect to the simplified model with a constant emissivity are well below the range of uncertainties. The nominal value of 0.4 is considered and a ±0.2 uncertainty will be considered in Section 3.2.3. 10 mm gaps in the GHe MLI located in-between the GHe panels and the LN_2 shield are considered. This will induce a direct heat load from the LN_2 shield and its MLI.

Regarding the emissivity of the silicon test mass, it is also subject to quite high uncertainties. Constancio et al. [36] derived some temperature-dependent emissivity models between 120 K and 260 K from measurement. The obtained curve is $\epsilon(T) = 0.00245T + 0.116$, giving an emissivity of 0.75 at 260 K and 0.41 at 120 K. Although not rigorous, extrapolating below 120 K to 40 K or even 20 K would lead to an emissivity of 0.2 or 0.16, respectively. As silicon exhibits semi-transparency in that part of the IR spectrum, bulk absorption is expected. The thickness of the silicon sample therefore plays a role, both for the absorption and emission of IR from the environment but also for the absorption of the laser beam in the Einstein Telescope. In the frame of the E-TEST project, a simplified model was collectively assumed with on a constant value 0.4.

The electrical harnesses coming from the marionette to the various thermal and mechanical sensors described in Section 2.4 are also modelled. They are discretised to capture the temperature gradient and related heat loads with the effect of the temperature-dependent thermal conductivity.

3.2. Baseline configuration

3.2.1. Nominal parameters

Fig. 14 gives the cooling profile of the suspended cryostat. The final expected steady-state temperature of the inner cryostat, cold platform and mirror is about 26.5 K with an outer cryostat actively cooled at 20 K. Considering the steady-state to be 1 K from the exact final steady-state temperature, the temperature of 27.5 K is achieved after 13 days of cooling which lies within the 20 days window allowed in the E-TEST project due to vacuum chamber availability. Analysing the heat flows of the suspended payload, given in Fig. 15, the total heat load is 366 mW with a major contribution (140 mW) from the modelled imperfections in the MLI. This is more than the 50 mW obtained in the preliminary assessment done in Section 2.2 since a gap of 10 mm in between the

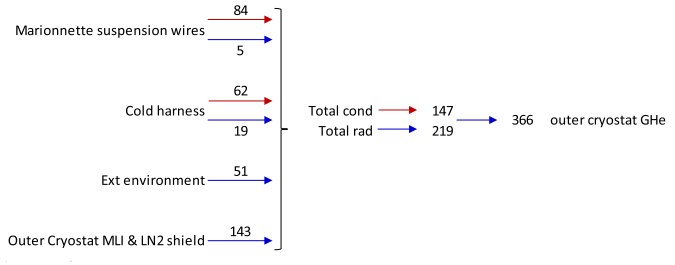

Fig. 15. Steady state heat flow map [mW]. Red and blue arrows indicate conductive and radiative heat flow, respectively.

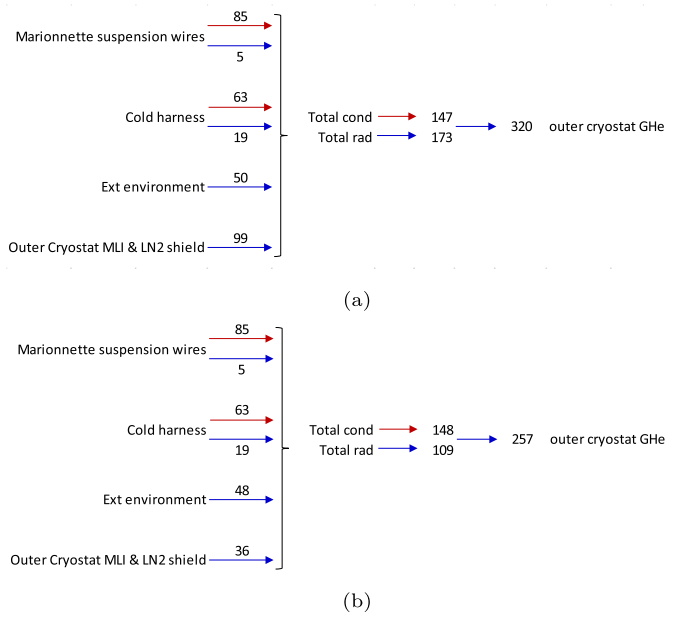

Fig. 16. Steady-state heat flow map [mW] considering (a): a reduced GHe MLI gap from 10 mm to 5 mm and (b) a completely closed GHe MLI gap. Red and blue arrows indicate conductive and radiative heat flow, respectively.

bottom and top halves of the GHe MLI gives a direct view to the LN_2 panels and their MLI. For the load coming from the 6 apertures, the 50 mW is in line with the assessment. The preliminary value of 100 mW from the suspension wire is also confirmed here with the 89 mW. The cold harnesses conductive contribution of 60 mW is not far from the initial 50 mW but an additional 20 mW of radiative contribution is present in the detailed model. The model is checked against Equation (1) since with a temperature of 26.5 K, a sink at 20 K and an emissivity of 0.4, the area of the heat exchanger is 78 m^2.

3.2.2. Sensitivity analysis

GHe MLI As it was highlighted in Section 2.2, the gap in the GHe MLI induces a significant contribution to the overall heat load. The effect of the reduction of the gap from 10 mm to 5 mm is thus analysed. Fig. 16a shows the updated heat flow map where the contribution is decreased by more than 40 mW for a total heat load of 320 mW instead of 366 mW. This translates into a gain of 0.5 K on the steady-state temperature of the mirror from 26.5 K to 26 K, which shows that the MLI integration must be performed with great care.

Closing the GHe MLI gap completely (without closing the gap between the GHe panels themselves so that the GHe MLI is still seen by the inner cryostat) results in another reduction of 60 mW to reach a total of 257 mW as described in Fig. 16b. It also further reduces the final steady-state temperature to 25.2 K. This highlights the importance of the insulation tightness surrounding the actively cooled GHe panels

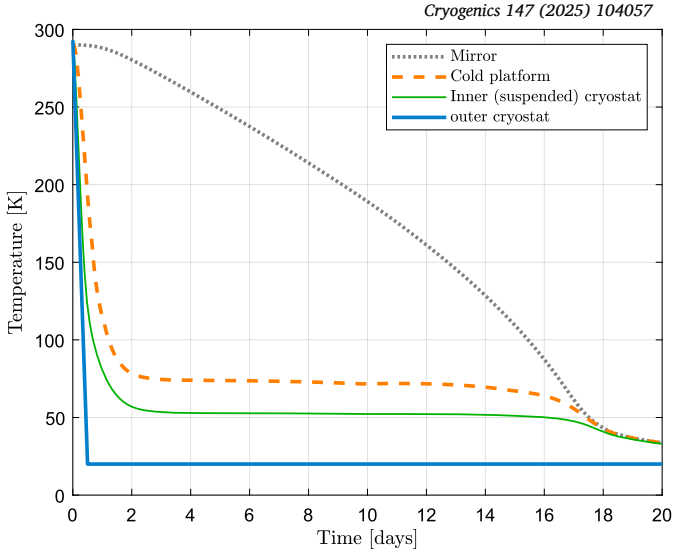

Fig. 17. Mirror, cold platform and inner suspended cryostat temperature profile considering no radiation of Silicon mirror (emissivity = 0).

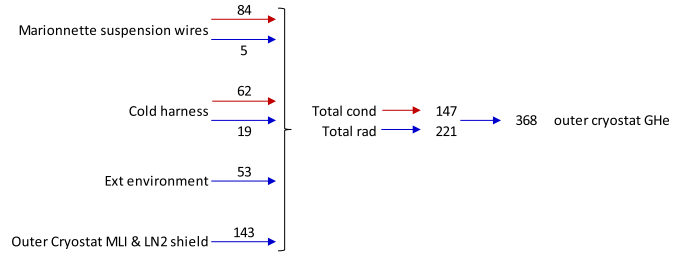

Fig. 18. Steady-state heat flow map [mW] considering no radiation of Silicon. Red and blue arrows indicate conductive and radiative heat flow, respectively.

of the external cryostat. The nominal10 mm gap leads to an additional 100 mW heat load.

Silicon mirror emissivity To assess the influence of the radiative cooling of the silicon mirror itself, the emissivity of the mirror is set to 0. Fig. 17 shows the resulting cooling profile and Fig. 18 the corresponding heat flow map. While the steady-state heat flow map is very similar to the one presented in Fig. 15 (since it does not show details of the mirror itself and the surface of the mirror is small with respect to the surface of the heat exchanger), the cooling profile is drastically different. The steady-state temperature (26.7 K) is not even achieved after 20 days. This highlights the importance of taking into account the mirror emissivity in cooling predictions.

3.2.3. Global uncertainty analysis

As already introduced above, uncertainties should be considered for the robustness of the predictions. Not only uncertainty on the black coating emissivity (±0.2) will be considered, but also:

- the thermal conductivity of the materials (±10%)
- the contact conductance between the different assemblies (±50%)
- the specific heat of the material (±10%)
- the emissivity of the rest of the components. This value depends on the nominal emissivity, and ±0.2 for the black paint and silicon emissivities was considered).

One worst and one best case are derived to envelope the nominal prediction. The results are given in Fig. 19. In the most optimistic case, the steady state temperature ends at 24.5 K while in the worst case it

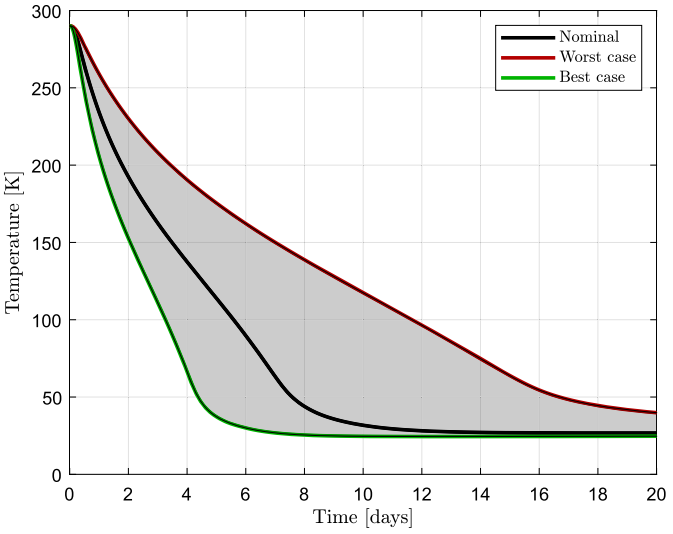

Fig. 19. Mirror temperature profile with nominal, worst and best assumptions regarding material properties.

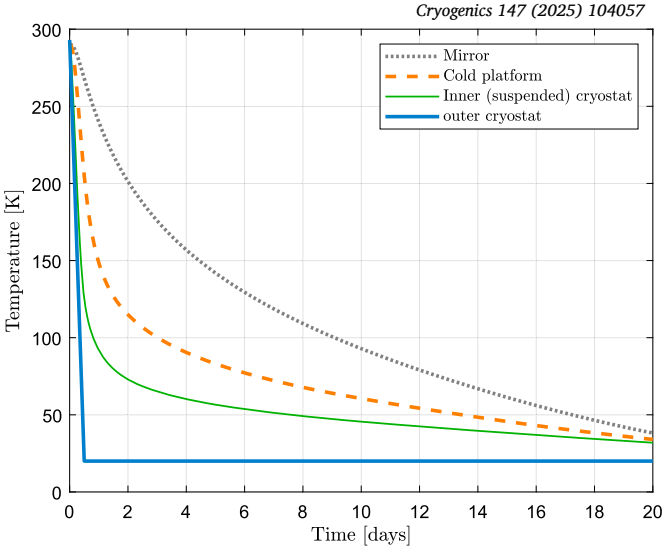

Fig. 20. Black aluminium mirror with CuCrZr suspension rods, cold platform and inner suspended cryostat temperature profile.

becomes 35 K. In the worst case, the time to cool down is largely increased and after 20 days, the temperature of the mirror is still about 40 K and is reaching 1 K above steady-state only after 25 days.

3.3. As-built configuration predictions

The final selected vacuum-compatible black coating is Aeroglaze Z307 with a targeted nominal thickness of 50 µm. As shown in Fig. 13, at the same thickness, it exhibits a higher emissivity than the classical Z306 version, usually used in spacecraft applications. As mentioned, the silicon mirror and suspension rods were replaced by an aluminium mirror and CuCrZr rods with 9 mm diameter and one thinner section (3 mm diameter) at each end acting as mechanical hinge. Replacing the 100 kg silicon mirror by 100 kg aluminium has a strong impact on the thermal behaviour since the specific heat of aluminium (900 J/kgK at 300 K) is larger than the one of silicon (700 J/kgK at 300 K). The emissivity is also lower, raw aluminium presenting an ambient emissivity of the order of 5% to 10%. Section 3.2.2 showed the importance of the radiation of the mirror on the cooling profile. To overcome this drawback, it was decided to paint the mirror with Aeroglaze Z307. Fig. 20 shows the resulting cooling profile. As expected, the cooling time increases significantly. After 20 days, the mirror does not reach steady-state and only achieves 38 K. As presented in Fig. 21, the steady sate heat flow map is however identical to the silicon version since the assumed value for the emissivity of the black paint is identical to the silicon one.

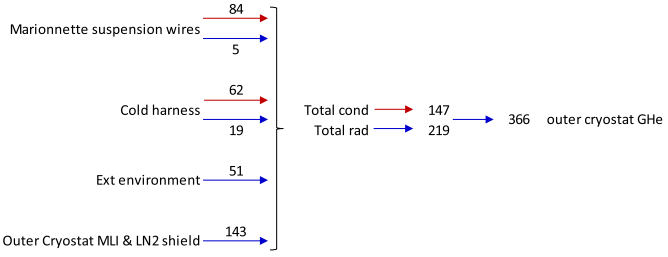

Fig. 21. Steady-state heat flow map of the as-built configuration [mW]. Red and blue arrows indicate conductive and radiative heat flow, respectively.

4. Prototype assembly and test results

4.1. Assembly and instrumentation

Between August and November 2023, the different sub-systems were assembled in the ISO7 cleanroom at CSL with the aim to test the prototype in the 6.5 m diameter vacuum chamber (FOCAL6.5).

After being painted, all the fins were integrated on the inner and outer cryostat. Fig. 22a shows the fins mounted onto the inner cryostat structure, before integration of the cold platform and mirror. The fins being very delicate, some of them suffered plastic deformation during assembly and painting. Some reinforcement was therefore added at the tip of the fin to retrieve sufficient flatness, as illustrated in Fig. 22a. One side of the inner cryostat was designed to be removed from the outside to give access for the integration of the mirror and the cold platform equipped with the sensors. Fig. 22b shows four inertial sensors mounted inside the inner cryostat. It also illustrates the copper braids

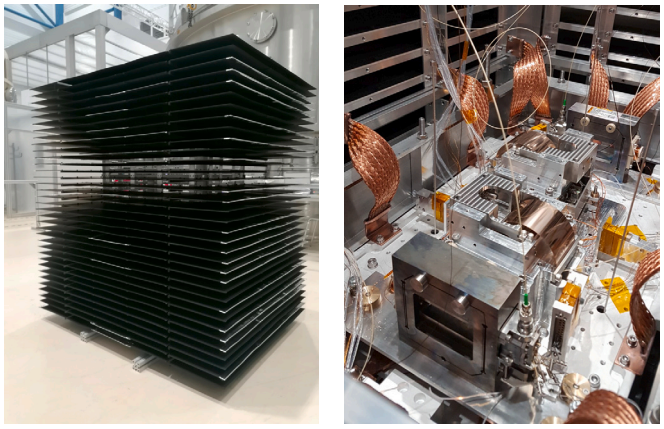

(a) (b)

Fig. 22. (a): Inner cryostat assembly waiting for the cold platform and mirror to be integrated. (b): Sensor plate, with two vertical sensors and two horizontal sensors integrated inside the inner cryostat.

(16 in total) ensuring the conductive coupling between the cold platform supporting the mirror and the inner cryostat structure onto which the fins are attached. The use of flexible copper braids allows mechanical decoupling between the cold platform, required for fine adjustment of the suspended payload centre of mass, as mentioned in Section 2.4.

In parallel of the inner cryostat and cold platform integration, the active platform, inverted pendulum and marionette were assembled. Once the active platform was mounted inside the chamber, preliminary fit

(a) (b)

Fig. 23. (a): Inner cryostat integrated below the inverted pendulum on the active platform. (b): Three sides of the outer cryostat integrated around the suspended inner cryostat.

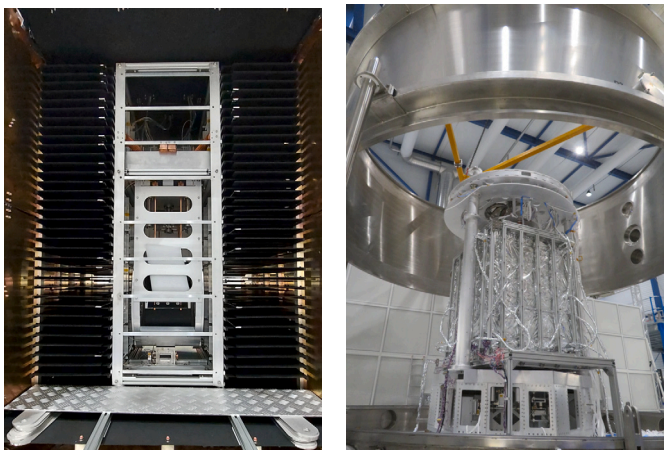

(a) (b)

Fig. 24. (a): Zoom on the outer and inner cryostat interleaved fins to check proper alignment and gap, before closing the last sides of the inner and outer cryostat. It also shows the horizontal inertial sensor located at the bottom of the inner cryostat. (b): Completed cryostat during the FOCAL6.5 vacuum chamber closing.

and suspension checks of the inner cryostat by the inverted pendulum were conducted, as illustrated in Fig. 23a. The sequence required then to temporarily remove the inverted pendulum to enable the integration of the first three lateral sides of the outer cryostat. The integration of the lateral sides of the outer cryostat required perfect horizontal alignment of the fins to allow the insertion in between the inner cryostat fins. This was conducted thanks to a dedicated hoisting device designed with adaptative counter-weighting, already illustrated in Fig. 5.

The inverted pendulum was then mounted back onto the active platform, with one side of the cryostat left open to perform the suspension of the inner cryostat to the marionette and inverted pendulum, as depicted in Fig. 23b. The optical and electrical harnesses routing along the suspension wire towards the outside of the cryostat are also performed at that moment. Fig. 24a illustrates the alignment check of the inner and outer fins.

The last side of the cryostat is eventually integrated, carefully aligning the fins and making sure the thermal insulation is properly installed. The chamber is finally closed, as depicted in Fig. 24b. The lateral door in the chamber vessel allowed last electrical checks before final closure and pumping.

Table 2
Cooling test key durations.

	100 K	50 K	Final T [K]
Suspended cryostat	< 1 day	4 days	21.6
Cold platform	1.5 day	5 days	21.6
Mirror	7 days	14 days	22.0

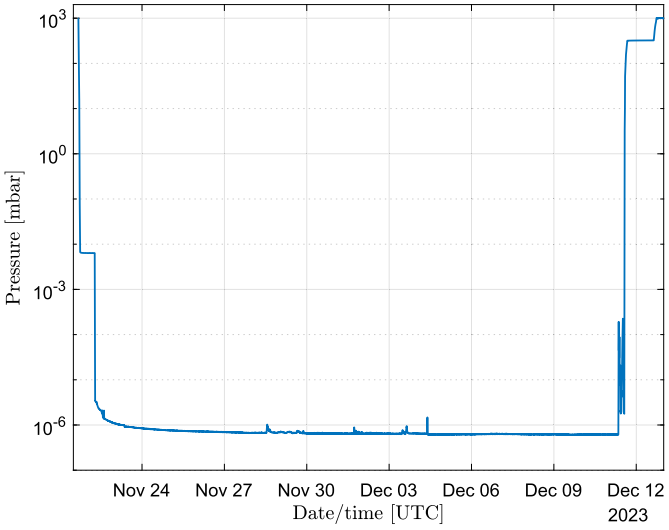

Fig. 25. Chamber pressure profile. Primary pumping started on the evening of November 21st and turbo pumping in the next morning, explaining the constant pressure during the night. The first phase of pressure recovery with dry nitrogen for the warm-up started on December 11th, followed by the second phase with air the next day.

To monitor the temperatures of the various components, the suspended payload was instrumented with 22 cryogenic Si435 temperature-monitoring diodes from Scientific Instrument. 14 are placed on the inner cryostat to monitor the uniformity of the structure. 2 diodes are mounted on each of the following items: mirror, inertial sensors, cold platform, and on the titanium wire suspension interface. On top of the temperature sensors of the suspended payload, 1 diode was also mounted on each of the 12 GHe-fed panels of the outer cryostat. LN_2 external panels were instrumented with standard Pt1000 temperature sensors.

4.2. Test chronology

The chamber was closed on November 21st, 2023 and primary pumping was started in the afternoon. Turbo pumping was then started in the morning of November 22nd. When pumping started, the buoyancy effect inducing a small downward translation of the suspended payload was observed through the reading of the displacement sensors on the IP top stage. The LN_2 shield was started slightly after the turbo pumping, once the pressure was below 10^{-5} mbar. After 2 hours, the LN_2 shield was around 90 K. In parallel, the helium refrigerator plant was started. The time required for the plant to be cold and feed cold gaseous helium to the cryostat is a few hours and the external cryostat Helium panels started to cool down around noon of November 23rd. In the morning of November 23rd, the external cryostat helium panels were below 30 K on average and the helium refrigerator return line was switched to a colder heat exchanger to finally reach an average temperature around 15 K. From that moment, the suspended cryostat and mirror radiative cool down started. Table 2 summarises the key duration of the cooling, highlighting that the mirror reached 50 K nine days after the cold platform. This already suggested that the CuCrZr suspension wires strongly contribute to the cooling bottleneck.

Therefore, the warm-up started in the morning of December 11th. The pumping was stopped around noon of December 11th. Fig. 25 shows

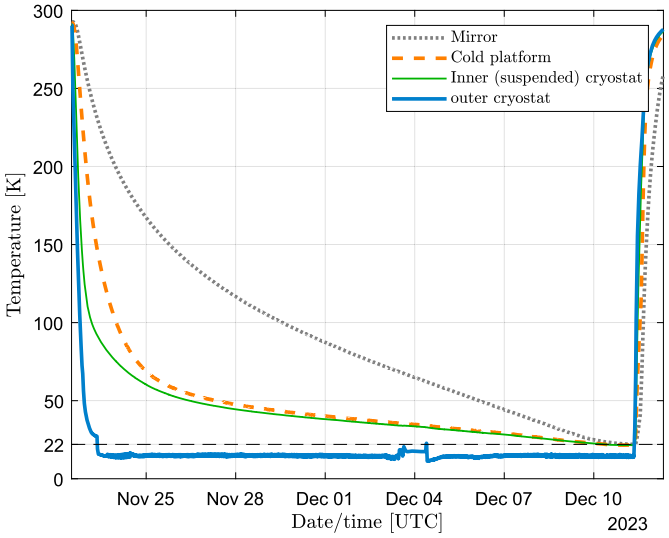

Fig. 26. Measured temperatures of the mirror and cryostat elements. The helium refrigerator was started on November 22nd, right after the LN_2 shield and warm-up started on December 11th right after reaching 22 K.

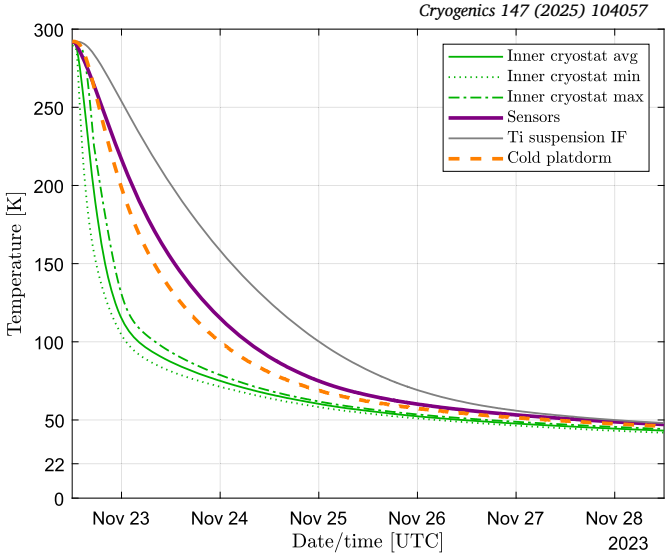

Fig. 27. First 6 days cooling profile of the suspended cryostat elements, highlighting the uniformity of the suspended part of the radiative heat exchanger (in green) even during transient. The cold platform, sensor and suspension interface catching back after 4 days.

the pressure profile obtained during the test. The achieved pressure in the chamber was 6×10^{-7} mbar partially thanks to cryo-pumping of the helium panels. The warm-up was conducted very carefully, to mitigate the classical pressure peaks arising from the desorption of the accumulated cryo-adsorbed gas on the panels. Partial pressure recovery to 300 mbar with dry nitrogen was then performed to induce convection and accelerate the warm up of the suspended payload. Final pressure recovery to ambient pressure with air was then performed once the mirror temperature was sufficiently high to avoid water condensation.

4.3. Temperature data

Fig. 26 presents the evolution of the average temperature of the main components of the setup. The actively GHe-cooled panels reached a temperature in the range of 14–15 K after 1 day. The small perturbation in the outer cryostat temperature observed around December 4th is due to some regeneration of the helium refrigerator plant. Its effect on the cooling profile is barely visible. From 50 K, the cold platform followed closely the inner cryostat structure. While the cold platform and inner cryostat crossed 50 K, the mirror was still above 120 K. The decrease of the specific heat of aluminium with temperature induced almost a linear trend in the mirror cooling profile between 100 K and the final landing at 22 K. The warm-up phase, thanks to the nitrogen pressure recovery allowing for convection to take place again and through the circulation of ambient GHe in the outer cryostat panel, took less than 1.5 days.

While Fig. 26 showed the average temperature of the different elements, Fig. 27 highlights that the temperature of the suspended cryostat is quite uniform. Yet, during the first part of the cool-down, above 100 K, the difference between the maximum and minimum measured temperature reaches 80 K. The top of the inner heat exchanger structure is colder than the bottom part during transient since the external cryostat panels are connected in series, the top panels being first fed with cold GHe, the bottom panels being the last ones to be cold. Below 100 K, the uniformity is better than 15 K and below 50 K, it drops to 2.5 K. In the end, the difference between the highest and lowest temperature of the inner cryostat is less than 0.5 K. The suspension interface, *i.e.* the lower extremity of the three titanium wires coming from the marionette being at ambient temperature outside the cryostat, is the warmest point during transient (except for the mirror) but quite rapidly merges with the rest of the suspended structure, showing that the radiative thermalisation of the wires through the entrances tubes is effective. The sensors, although not strongly conductively linked to the cold platform, also followed smoothly the cooling, thanks to radiative heat exchanges, finally also hitting the 22 K. Conduction heat load through electrical and optical harnesses was thus well minimised through the thermalisation tubes. It also confirms the low thermal dissipation of the sensors.

5. Model correlation

Although the model with the nominal parameters predicted that the payload could not reach stability after 20 days of cooling, the test results were eventually more satisfactory. The comparison of Figs. 26 and 20 already shows several leads for the correlation of the model:

- First the temperature of the GHe-fed panels, cooled by the helium refrigerator and acting as boundary condition in the model, is slightly lower than expected (15 K instead of 20 K).
- Second, the cold platform follows the inner cryostat temperature much more closely than predicted (around 50 K after 6 days instead of 75 K).
- Finally, the mirror cools slightly faster than expected and reaches stabilisation around 22 K.

The main parameters that required small adjustment in the model are the measured masses of cold platform sensors, the actual number of electrical harness, the copper braids final length and thermal contact and finally the emissivity of the Aeroglaze Z307 black paint increased to 0.65, playing a major role. Fig. 28 presents the correlation results, eventually fitting pretty well the measured data. The warm-up phase is not considered in the correlation since convection was artificially induced as explained above.

Although the correlated model provides quite a good match with the measured data, it remains difficult to discriminate the effect of the emissivity of the black paint from some imperfections in the insulation (MLI) of the cryostat. Indeed, the model still includes some imperfection (gaps) in the MLI surrounding the cryostat, inducing parasitic heat load as described in Section 3.2.3. If the MLI was indeed more efficient that considered in the model, therefore reducing the heat load on the payload, a different (smaller) black paint emissivity would lead to the same results.

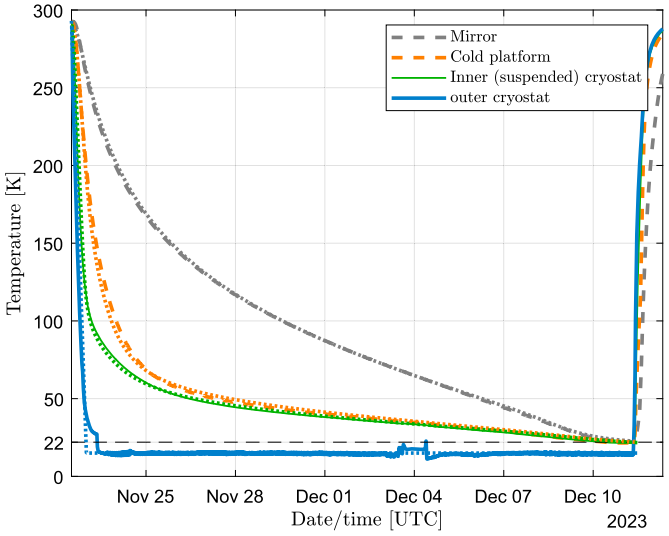

Fig. 28. Comparison of test data and correlated model. Dotted lines correspond to correlated ESATAN model.

6. Conclusions and future work

The paper presented the design and operation of an innovative cryostat, capable to extract heat of a large payload in a purely radiative way. The main advantage of this technology is the contact-free nature of the radiative heat exchange, which is not expected to induce any vibration, making it particularly suitable to cool down sensitive payloads like the heavy mirrors of future gravitational wave detectors. The low-vibration nature of the cooling strategy will be investigated in a dedicated publication.

Based on specifications derived from the ones of the Einstein Telescope, a cryostat was designed, produced and assembled. Its cooling capability was tested with an aluminium test mass, representative of one mirror of the ET-LF (low frequency).

A test campaign was conducted, where the temperature was monitored at various locations during the cooling phase. Experimental results were found to match closely with theoretical prediction, both in terms of cooling rate and asymptotic values. After 19 days, the payload temperature stabilised at 22 K. These encouraging results demonstrate that the proposed strategy has a strong potential to be implemented in the final design of ET-LF cryostat.

The next step for the E-TEST prototype is to change the aluminium mass for an ET-like 450 mm silicon mirror. The design of silicon mirror suspension is also left for future work.

The outcome of the E-TEST campaign highlighted multiple points of interest. One of the most important is the necessity for system engineering to ensure all disciplines and constraints are considered throughout the design. The design of such complex systems, in particular at the scale of the ET, would really benefit from a concurrent engineering process, similar to what is done for space missions with the Concurrent Design Facility of the European Space Agency [37,38]. Another important aspect is the importance of considering the integration process early in the design phase. On that topic, it is planned to re-assess the overall architecture of the cryostat, considering again the trade-off between vertical and horizontal stacking of the fins. Circular vertical interlocking could also be envisaged, relaxing the yaw degree of freedom (rotation around the vertical axis) and enabling vertical integration.

Emissivity enhancement at low temperature is also a key to enabling further reduction in the temperature or required area. Micro-structuring with corrugated or honeycomb-like structure could offer higher emissivity at low temperature but could also contribute to the stiffness of the fin. The lack of accurate data regarding thermo-optical properties at low temperature was also highlighted and this matter will be investigated. The effect of having an even colder outer cryostat, for instance cooled to liquid helium temperature should also be assessed. In the present project, MLI was used as default and easily available insulating material but shall be prohibited in the ET due to the large moisture release. Alternatives, for instance developed for space telescope sensitive to contamination, shall be considered.

Finally, the dynamic behaviour and thermal noise induced by the suspended part of the radiative heat exchanger attached to the cold platform was not covered by this paper and shall also be assessed.

The investigations described above will help improving the design of the E-TEST cryostat and its cryogenic radiative heat exchanger and pave a way towards the ET-LF cryostat design.

CRediT authorship contribution statement

Lionel Jacques: Writing – original draft, Supervision, Methodology, Formal analysis, Conceptualization. **Morgane Zeoli:** Writing – original draft. **Anthony Amorosi:** Writing – review & editing, Resources. **Alessandro Bertolini:** Writing – review & editing, Resources. **Christophe Collette:** Writing – review & editing, Supervision, Methodology, Investigation, Funding acquisition, Conceptualization. **Robin Cornelissen:** Resources. **Chiara Di Fronzo:** Writing – review & editing, Resources. **Serge Habraken:** Resources. **Joris V. van Heijningen:** Resources. **Gino Hoft:** Resources. **Robert Joppe:** Resources. **Tim J. Kuhlbusch:** Resources. **Mouhamad Haidar Lakkis:** Resources. **Bao Long Levan:** Resources. **Cédric Lenaerts:** Supervision, Resources, Project administration, Investigation. **Jérôme Loicq:** Project administration, Funding acquisition. **Benoit Marquet:** Resources. **Enrico Porcelli:** Resources. **Ameer Sider:** Resources. **Matteo Tacca:** Writing – review & editing, Resources.

Declaration of competing interest

The authors declare the following financial interests/personal relationships which may be considered as potential competing interests: Christophe Collette reports financial support was provided by Interreg V-A Euregio Meuse-Rhine Programme. This work comes within the scope of the E-TEST project, which is carried out within the framework of the Interreg V-A Euregio Meuse-Rhine Programme, with €7,5 million from the European Regional Development Fund (ERDF). By investing EU funds in Interreg projects, the European Union is investing directly in economic development, innovation, territorial development, social inclusion, and education in the Euregio Meuse-Rhine region. For a thorough review, the authors would like to thank European Union for this support and investment. The authors gratefully acknowledge the European Research Council, Consolidator grant SILENT (grant agreement number 866259), and the Fonds National de la Recherche Scientifique (FNRS), projet de recherche STELLAR (T.0022.22), for funding this research. If there are other authors, they declare that they have no known competing financial interests or personal relationships that could have appeared to influence the work reported in this paper.

Acknowledgements

This work comes within the scope of the E-TEST project, which is carried out within the framework of the Interreg V-A Euregio Meuse-Rhine Programme, with €7,5 million from the European Regional Development Fund (ERDF). By investing EU funds in Interreg projects, the European Union is investing directly in economic development, innovation, territorial development, social inclusion, and education in the Euregio Meuse-Rhine region. For a thorough review, the authors would like to thank European Union for this support and investment. The authors gratefully acknowledge the European Research Council, Consolidator grant SILENT (grant agreement number 866259), and the Fonds National de la Recherche Scientifique (FNRS), projet de recherche STELLAR (T.0022.22), for funding this research. The document is referenced in the ET database under the code ET-0708A-24.

Appendix A. Preliminary heat load assessment

The main sources of heat to be evacuated from the mirror and cold platform are:

- Radiative heat load from nominal apertures (suspension wires, optical apertures)
- Radiative heat load from holes & defects in MLI
- Conductive heat load from the suspension wires
- Conductive heat load from the payload electrical harness (temperature sensors, vibration sensors)

Aperture radiative heat load The radiative heat load through the 6 apertures providing direct view to ambient can easily be assessed and is of the order of 50 mW for 6 tubes, considering 30 mm diameter and 300 mm long tubes (ratio 10 to limit the view factor) and assuming an internal emissivity of 50% and specular reflection. Multiple reflections inside the tubes are taken into account as they play a significant role. Increasing the internal reflectivity of the tube, especially if specular, largely increases the heat load. If the reflection is diffuse, the heat load is decreased by a factor 10, down to 5 mW. If the reflectivity goes up to 80% instead of 50%, the heat load increases to 8 mW for diffuse reflections but to almost 300 mW for specular reflections.

Insulation radiative leaks The GHe panels do not provide a perfectly tight thermal environment and some heat load could still leak through the gaps in between different panels. The gaps give a direct view to the MLI located in between the GHe panels and the LN_2 thermal shield. The 10-layer MLI used at CSL itself provides an insulation of the order of 20 mW/m^2 between 80 K and 4 K. Considering conservatively some imperfection in the MLI (performance degradation of 150% to 50 mW/m^2), it still allows 1 m^2 of apertures through the GHe envelope for a budget of 50 mW, if the MLI is itself tight.

Suspension wire conductive heat load The suspension wires are made of titanium which is a good metallic thermal insulator with a thermal conductivity around 7 W/mK at ambient temperature, dropping to 1 W/mK at 20 K. The three wires have a diameter of 3 mm to support the weight of the payload. To assess the heat load from the suspension wires, an effective temperature gradient length of 250 mm is assumed. Taking an average thermal conductivity of 4 W/mK, the heat load through the suspension wires is about 100 mW.

Electrical harnesses conductive heat load Finally, the heat load through the electrical harness of the cryo-sensors can be assessed. High-thermal resistance cables are assumed, such as Phosphor Bronze having a thermal conductivity of 50 W/mK at ambient temperature and 10 W/mK at 20 K. Small cross section wires for signals and larger cross section ones for power are also assumed: 150 × AWG32 and 5 × AWG24 would lead to an additional 50 mW heat load. The harness is thermally anchored by being twisted around the cold platform suspensions and surrounded by baffling tubes to reduce its radiative and conductive heat load contribution. To avoid transmitting vibration to the payload and further, the harness stiffness is decreased by routing it forming U-shape bellows between their vibrating origin and the low-vibrating marionette from which departs the suspension wires. Joule effect in the harness is neglected as the current are expected to be very small. Conduction through optical fibres connected to the vibration sensors is also neglected as the thermal conductivity of optical fibres is also very low (<1 W/m/K).

Summary and required heat exchanger area The total heat load to the payload can be estimated to around 250 mW, as summarized in Table A.3.

Table A.3
Heat load assessment summary.

	Q [mW]
Apertures	50
MLI leaks	50
Suspension wires	100
Harness	50

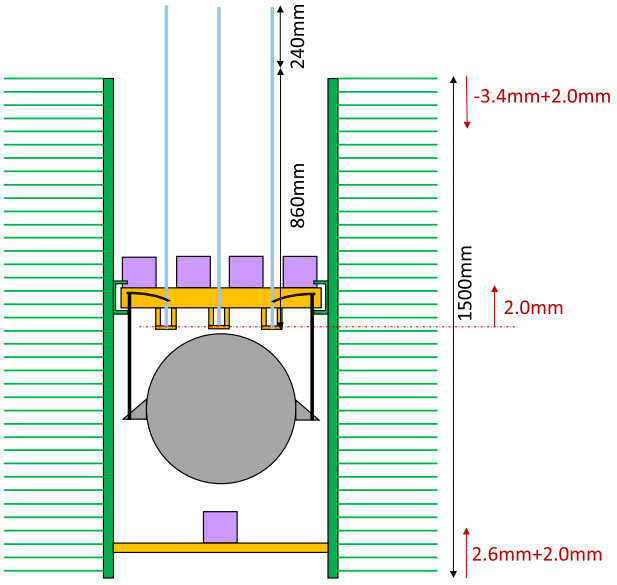

Fig. B.29. Inner cryostat global thermal contraction showing a global rise of the suspended payload.

Appendix B. Detailed considerations for the inter-fin gap sizing

Several contributors constrain the required clearance between the internal and external fins.

Suspended radiative heat exchanger global shrinkage and rise The suspended radiative heat exchanger structure is completely made of aluminium, selected for its light weight and excellent thermal conductivity. However, aluminium also exhibits a quite high coefficient of thermal expansion (CTE), contraction in the present case. Between ambient temperature and 20 K, aluminium will contract by about 4 mm per meter. Being 1.5 m tall, the structure will contract by about 6 mm. As the inner cryostat is suspended by titanium rods whose ends are 860 mm away from the top of the inner cryostat, it will shrink around that level. Titanium contraction is less than aluminium and is about 1.8 mm/m between ambient and 20 K. This means that due to the contraction of the titanium wires, the attachment point of the payload will move up by about 2 mm with respect to the outer cryostat. In total, the top of the suspended radiative heat exchanger structure will go down by about 1.4 mm and the bottom will go up by about 4.6 mm, as illustrated in Fig. B.29. Temperature gradients in transient and in steady-state are expected to be low so that homothetic shrinkage is assumed.

Thermo-elastic analyses of the outer cryostat Regarding the outer part of the cryostat, the use of several different materials, mainly the fin structure made of aluminium and the GHe panels made of copper, does inevitably introduce large distortions. To mitigate these effects, the copper panel is sandwiched in-between the aluminium fin structure and an additional aluminium bar at the back of the panel. This helps to keep the GHe panel flat. Fig. B.30 shows the resulting thermo-elastic displacement obtained from finite element analysis (FEA). The model includes the PCTFE blades supporting the LN_2 shield panel, the PCTFE blades

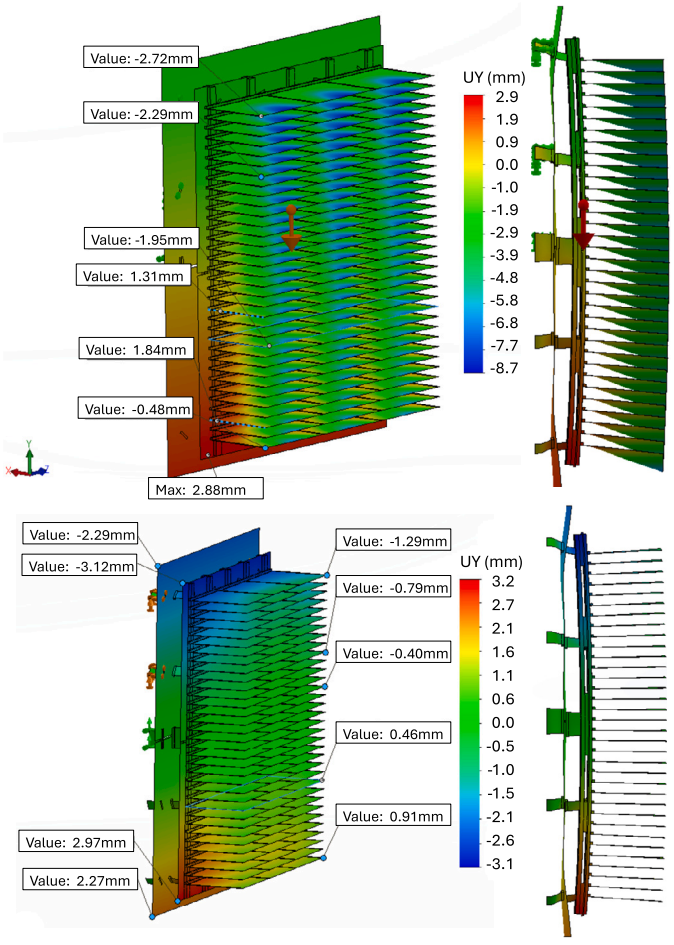

Fig. B.30. Outer cryostat thermo-elastic vertical displacement from FEA. Top Figure includes both gravity and thermo-elastic effects and bottom only thermo-elastic deformation.

between the LN_2 panels and the GHe panels and the fin structure. Gravity is also included in the model and in the results shown in the top of Fig. B.30.

Overall, the GHe panel contracts by 6 mm around the centre. However, some bending counteracts the contraction and the tip of the fins only moves towards the centre by about 1 mm. Still, the base of the top and bottom fins is moving by about 3 mm towards the centre. The choice of copper for the panels is mainly historical for compatibility with CSL existing facilities. The design could be improved by using aluminium for the panels as well. Aluminium with TIG welded aluminium tubes is actually the standard choice for thermal shroud panels in US spacecraft testing facilities [39]. Some thermo-elastic bending of the fins is also to be expected since the CTE of the black paint is different from the one of aluminium and the target thickness of the paint (50 µm) is not negligible with respect to the thickness of the fin (200 µm). No data was available regarding the paint CTE. Stress relaxation from manufacturing is also to be expected.

Manufacturing and assembly tolerances On top of the predictive deformations, many statistical contributors also affect the gap between the fins. A non-exhaustive list of contributors is exposed here below:

- Global tilt of the suspended radiative heat exchanger with respect to the outer cryostat due to mis-balancing. Over the 1400 mm span of the inner cryostat from tip to tip, 1 mm in each direction is already a reasonable target after adjustment.
- Offset in the positioning of the fins inside their mounting holes: the through-hole is always larger than the screw diameter. Each fin could therefore be mounted either 0.5 mm above or below its nominal position.
- Offset in the fin clamping. The perpendicularity of the fins is ensured by the squareness of the 10×10 rods linking the fin fork support to the vertical T-shape profile. Manufacturing tolerances of the 10×10 rods, according to ISO EN754-4 ensure the side length does not deviate more than 50 µm. For a 300 mm long fin, this leads to a maximum deviation of 1.5 mm at the tip.
- Fin foil flatness. The manufacturing and assembly technique inevitably induces deflection in the foil. A target of 2 mm flatness is allocated.

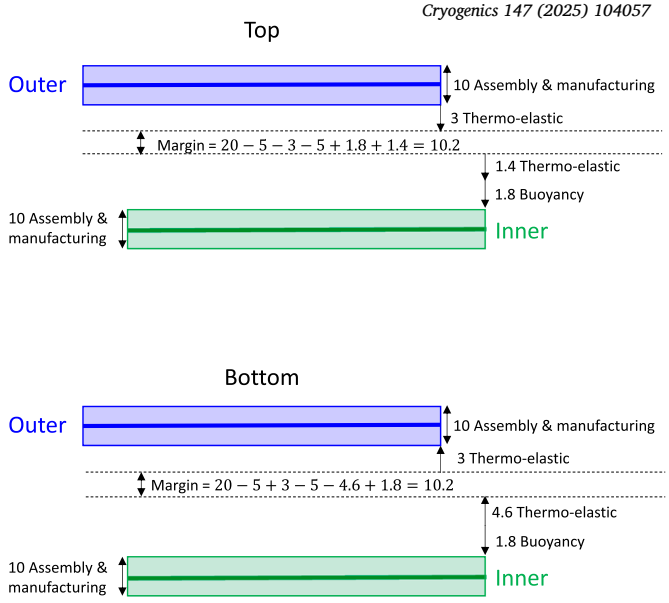

Fig. B.31. Inter-fin gap tolerancing analysis summary for the top and the bottom of the radiative heat exchanger [mm].

Buoyancy effects The inner cryostat being suspended and in equilibrium, when the air is pumped out of the vacuum chamber, removes the vertical force due to Archimedes' law, directed upwards and equal to the removed volume of the inner cryostat and marionette. The stiffness of the GAS filter being 783 N/mm *i.e.* 12.5 mm/kg and the volume of the suspended cryostat including the marionette being 0.12 m^3, the suspended payload is expected to move down by 1.8 mm with respect to the top stage of the inverted pendulum. Similarly, the whole inverted pendulum is also suspended on the springs of the active platform, having a stiffness of 418 000 N/mm, *i.e.* 23.5 µm/kg. The volume of the suspended part of the active platform, inverted pendulum and inner cryostat being 1.1 m^3, an additional motion of 30 µm is expected.

Summary The various contributions to the distance between the suspended and external fins of the exchangers are summarised in Fig. B.31. In total, considering the allocated clearance of 20 mm between the fins, a margin of 10 mm is expected since the buoyancy effect almost cancels the one of the titanium suspension rods.

Data availability

Data will be made available on request.

References

[1] The LIGO Scientific Collaboration. Advanced LIGO. Class Quantum Gravity 2015;32:074001. https://doi.org/10.1088/0264-9381/32/7/074001.
[2] Acernese F, et al. Advanced Virgo: a second-generation interferometric gravitational wave detector. Class Quantum Gravity 2014;32:024001. https://doi.org/10.1088/0264-9381/32/2/024001.

[3] Abe H, et al. The current status and future prospects of kagra, the large-scale cryogenic gravitational wave telescope built in the kamioka underground. Galaxies 2022;10. https://doi.org/10.3390/galaxies10030063.
[4] Einstein Telescope Steering Committee Editorial Team. Design report update 2020 for the Einstein telescope. Technical report. 2020. ET-0007B-20.
[5] Nawrodt R, et al. Investigation of mechanical losses of thin silicon flexures at low temperatures. Class Quantum Gravity 2013;30:115008. https://doi.org/10.1088/0264-9381/30/11/115008.
[6] Adhikari RX, et al. A cryogenic silicon interferometer for gravitational-wave detection. Class Quantum Gravity 2020;37:165003. https://doi.org/10.1088/1361-6382/ab9143.
[7] Lyon KG, et al. Linear thermal expansion measurements on silicon from 6 to 340 k. J Appl Phys 1977;48:865–8. https://doi.org/10.1063/1.323747.
[8] Middelmann T, et al. Thermal expansion coefficient of single-crystal silicon from 7 k to 293 k. Phys Rev B 2015;92:174113. https://doi.org/10.1103/PhysRevB.92.174113.
[9] Puppo P, Ricci F. Cryogenics and Einstein telescope. Gen Relativ Gravit 2011;43:657–69. https://doi.org/10.1007/s10714-010-1037-x.
[10] Yamada T, et al. High performance thermal link with small spring constant for cryogenic applications. Cryogenics 2021;116:103280. https://doi.org/10.1016/j.cryogenics.2021.103280.
[11] Tomaru T, et al. Vibration analysis of cryocoolers. Cryogenics 2004;44:309–17. https://doi.org/10.1016/j.cryogenics.2004.02.003.
[12] Dubielzig T, et al. Ultra-low-vibration closed-cycle cryogenic surface-electrode ion trap apparatus. Rev Sci Instrum 2021;92:043201. https://doi.org/10.1063/5.0024423.
[13] Micke P, et al. Closed-cycle, low-vibration 4 K cryostat for ion traps and other applications. Rev Sci Instrum 2019;90:065104. https://doi.org/10.1063/1.5088593.
[14] Tomaru T, et al. Vibration-free pulse tube cryocooler system for gravitational wave detectors, part I: vibration-reduction method and measurement. In: Ross RG, editor. Cryocoolers 13. Boston, MA: Springer US; 2005. p. 695–702.
[15] Ikushima Y, et al. Ultra-low-vibration pulse-tube cryocooler system – cooling capacity and vibration. Cryogenics 2008;48:406–12. https://doi.org/10.1016/j.cryogenics.2008.04.001.
[16] Shapiro B, et al. Cryogenically cooled ultra low vibration silicon mirrors for gravitational wave observatories. Cryogenics 2017;81:83–92. https://doi.org/10.1016/j.cryogenics.2016.12.004.
[17] Utina A, et al. ETpathfinder: a cryogenic testbed for interferometric gravitational-wave detectors. Class Quantum Gravity 2022;39:215008. https://doi.org/10.1088/1361-6382/ac8fdb.
[18] Xhahi A, et al. Conceptual design of a sorption-based cryochain for the etpathfinder. Cryogenics 2023;134:103717. https://doi.org/10.1016/j.cryogenics.2023.103717.
[19] Burger J, et al. Vibration-free 5 k sorption cooler for esa's Darwin mission. Cryogenics 2002;42:97–108. https://doi.org/10.1016/S0011-2275(02)00008-5.
[20] Busch L, Grohmann S. Conceptual layout of a helium cooling system for the Einstein telescope. IOP Conf Ser, Mater Sci Eng 2022;1240:012095. https://doi.org/10.1088/1757-899X/1240/1/012095.
[21] Sider A, et al. E-TEST: a compact low-frequency isolator for a large cryogenic mirror. Class Quantum Gravity 2023;40:165002. https://doi.org/10.1088/1361-6382/ace230.
[22] Sider A, et al. E-TEST prototype design report. Available from: arXiv:2212.10083, 2022.
[23] Honig R, Hook H. Vapor pressure data for some common gases. RCA Rev 1960;21:360–8.
[24] Umrath W. Fundamentals of vacuum technology, Oerlikon Leybold vacuum; 1998.
[25] Corruccini R. Gaseous heat conduction at low pressures and temperatures. Vacuum 1959;7–8:19–29. https://doi.org/10.1016/0042-207X(59)90766-3.
[26] Malroy ET. Free molecular heat transfer programs for setup and dynamic updating the conductors in thermal desktop. In: Thermal and fluids analysis workshop; 2007.
[27] Grodent C, et al. Wide range thermal test facility for juice large appendages, design and results. In: Proceedings of the European conference on spacecraft structures, materials and environmental testing - ECSSMET 2018. ESA; May 2018.
[28] Marquardt ED, Le JP, Radebaugh R. Cryogenic material properties database. Boston, MA: Springer US; 2002. p. 681–7.
[29] Touloukian YS, et al. Thermophysical properties of matter - the TPRC data series. Technical Report. Purdue Univ., Thermophysical and Electronic Properties Information Center; 1975.
[30] Rambure N. Mesure des propriétés thermo-optiques aux températures extrêmes. Ph.D. thesis. Université Paris Ouest - Nanterre La Défense; 2010. 2010PA100093.
[31] Kauder L. Spacecraft thermal control coatings references, NASA/TP-2005–212792. Technical Report. Greenbelt, MD: NASA Goddard Space Flight Center; 2005.
[32] Rev T, et al. Emissivity of black coatings from ambient to cryogenic temperatures: how spectrally flat black coatings can enhance performance of space systems. In: Thermal & fluids analysis workshop, TFAWS. Greenbelt, MD: NASA Goddard Space Flight Center; 2023.
[33] Tuttle J, Canavan E. Recent NASA/GSFC cryogenic measurements of the total hemispheric emissivity of black surface preparations. IOP Conf Ser, Mater Sci Eng 2015;102:012015. https://doi.org/10.1088/1757-899X/102/1/012015.
[34] Tuttle J, et al. The area-density-dependence of ball ir black's low-temperature emissivity. Cryogenics 2014;64:240–3. https://doi.org/10.1016/j.cryogenics.2014.04.024.
[35] Renbarger M. Properties of ball InfraRed black, a new cryogenic thermal control coating. In: Straka SA, Carosso N, editors. Optical system contamination: effects, measurements, and control 2010. International Society for Optics and Photonics, vol. 7794. SPIE; 2010. p. 77940F.
[36] Constancio Jr M, et al. Silicon emissivity as a function of temperature. Int J Heat Mass Transf 2020;157:119863. https://doi.org/10.1016/j.ijheatmasstransfer.2020.119863.
[37] Bandecchi M. Concurrent design for innovative capacity building. Cham: Springer International Publishing; 2020. p. 357–75.
[38] Bandecchi M, et al. The ESA / ESTEC concurrent design facility. In: Proceedings of EuSEC; 2000. Available from: https://api.semanticscholar.org/CorpusID:174789939.
[39] Ash GS. Manufacture of cryoshroud surfaces for space simulation chambers. In: 25th space simulation conference. Environmental testing: the Earth-space connection; 2008.